Merging Metabolic Modeling and Imaging for Screening Therapeutic Targets in Colorectal Cancer

Niki Tavakoli[1+], Emma J. Fong[2+], Abigail Coleman[2], Yu-Kai Huang[2], Mathias Bigger[2,3], Michael E. Doche[2], Seungil Kim[2], Heinz-Josef Lenz[6], Nicholas A. Graham[3], Paul Macklin[4], Stacey D. Finley[1,3,5,*], Shannon M. Mumenthaler[1,2,6*]

[1] Alfred E. Mann Department of Biomedical Engineering, University of Southern California, Los Angeles, CA, 90089, USA
[2] Ellison Institute of Technology, Los Angeles, CA, 90064, USA
[3] Mork Family Department of Chemical Engineering and Materials Science, University of Southern California, Los Angeles, CA, 90089, USA
[4] Department of Intelligent Systems Engineering, Indiana University, Bloomington, IN, 46202, USA
[5] Department of Quantitative and Computational Biology, University of Southern California, Los Angeles, CA, 90089, USA
[6] Division of Medical Oncology, Norris Comprehensive Cancer Center, University of Southern California, Los Angeles, CA, 90033, USA
+Denotes co-first authors
*Co-correspondence: sfinley@usc.edu (S.D.F.), smumenthaler@eit.org (S.M.)

Keywords: *systems biology, metabolic modeling, fluorescence lifetime imaging microscopy, colorectal cancer, cancer associated fibroblast, tumor metabolism, drug resistance, tumor microenvironment*

Summary

Cancer-associated fibroblasts (CAFs) play a key role in metabolic reprogramming and are well-established contributors to drug resistance in colorectal cancer (CRC). To exploit this metabolic crosstalk, we integrated a systems biology approach that identified key metabolic targets in a data-driven method and validated them experimentally. This process involved high-throughput computational screening to investigate the effects of enzyme perturbations predicted by a computational model of CRC metabolism to understand system-wide effects efficiently. Our results highlighted hexokinase (HK) as one of the crucial targets, which subsequently became our focus for experimental validation using patient-derived tumor organoids (PDTOs). Through metabolic imaging and viability assays, we found that PDTOs cultured in CAF conditioned media exhibited increased sensitivity to HK inhibition. Our approach emphasizes the critical role of integrating computational and experimental techniques in exploring and exploiting CRC-CAF crosstalk.

Introduction

Tumor metabolism, recognized as a hallmark of cancer, is increasingly garnering attention as an avenue for therapeutic intervention.[1–3] A number of metabolic vulnerabilities have been identified; however, to date, efforts to bring metabolism-based drugs to the clinic have shown limited success. A significant hurdle lies in the intricate metabolic interplay within tumors, particularly the interactions between cancerous cells and nonmalignant cells within the tumor microenvironment (TME).[4] For example, studies have demonstrated a co-survival relationship between tumor cells and cancer associated fibroblast (CAFs), highlighting reciprocal interactions involving nutrient secretion and consumption.[5] This metabolic reprogramming has been shown to support tumor growth and drug resistance.[6–8] Given this complexity, utilizing a systems biology approach that combines high-throughput computational and experimental techniques is beneficial, as recently reviewed in Curvello *et al*.[9]

In the context of tumor metabolism, modeling has produced relevant quantitative insights in previous work.[10] Metabolic modeling encompasses various different techniques, each with its unique applications and insights.[11] One such technique is kinetic modeling, which simulates the dynamics of a system, predicting how the metabolite concentrations and reaction rates evolve over time. For example, in pancreatic cancer research, kinetic models have been fitted to experimental data to gain deeper insights into the network dynamics and perform enzyme knockdowns to identify ways to inhibit cancer cell proliferation.[12] Agent-based modeling is a technique that represents individual cells interacting with the TME and has been used to show metabolic changes under different environments.[13] Another technique is multi-scale modeling, which spans various spatial and temporal scales, offering a comprehensive view of biological processes. Such models incorporate intracellular models of metabolism to inform cell- and tissue-level behaviors.[14,15] Lastly, constraint-based modeling stands out as a widely adopted form of metabolic modeling. This technique works by predicting the flux distributions within a network by applying a series of constraints, allowing for the exploration of metabolic behaviors under different physiological and pathological conditions. Notably, constraint-based models can incorporate multi-omics data to generate context-specific models.[16–18] Additionally, performing flux balance analysis[19] using a constraint-based model of metabolism can predict enzymes that are the most essential to target and exploit.[20]

The current work builds upon our previous study of the mechanisms underlying the metabolic relationship between tumor cells and CAFs in the context of colorectal cancer (CRC).[21] By integrating metabolomics data and predefined experimental growth rates, constraint-based modeling revealed distinct ways in which CAFs specifically reprogram the central carbon metabolism of CRC cells. Notably, the presence of CAFs resulted in a significant upregulation of glycolysis, inhibition of the tricarboxylic acid (TCA) cycle and a disconnection in the oxidative and non-oxidative arms of the pentose phosphate pathway (PPP). The study also found distinct CAF-mediated alterations in glutamine metabolism. In addition, we applied the model to identify metabolic perturbations that uniquely inhibit growth of CRC cells in CAF-conditioned media (CAF-CM), compared to their original media. While informative, this prior work focused on how the perturbations influence cell growth, without considering the effects on other intracellular metabolic reactions. Furthermore, we did not experimentally validate the predicted targets.

In this current study, we significantly expand on our prior work to exploit the metabolic relationship between CRC cells and CAFs. We developed a systems biology workflow (**Figure 1**) for high throughput computational screening aimed at identifying metabolic perturbations that could serve as potential druggable targets. Using representation learning to reduce the dimensionality of our data[22], we performed a series of *in silico* enzyme knockdowns and analyzed their effects on each reaction in the metabolic network. Among the identified potential targets, hexokinase (HK) became our perturbation of interest to experimentally validate. This experimental validation was performed using 3D patient-derived tumor organoids (PDTOs), a physiologically relevant cell culture model system that has been shown to recapitulate the genetic and phenotypic properties of the original tumor.[23–25] We assessed drug responses using conventional cell viability assays and metabolic imaging techniques, namely fluorescence lifetime imaging microscopy

(FLIM)[26,27], to validate HK as a promising druggable target within the tumor microenvironment (TME). This refined focus underscores the unique metabolic dependencies created by CAF-conditioned media and emphasizes the need for our systems biology approach in uncovering the most promising therapeutic interventions for CRC in the TME.[28]

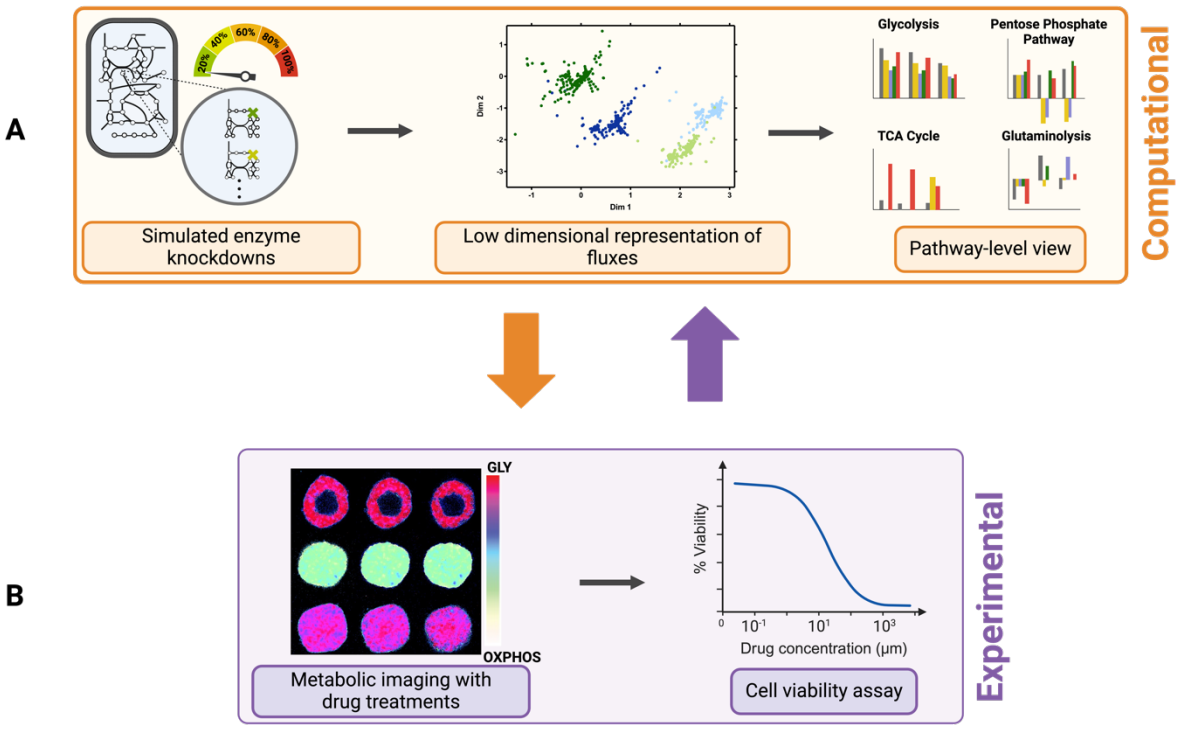

Figure 1: Project pipeline. (A) Computational portion of the study; for each culture condition, metabolic reactions were subjected to incremental knockdowns. We then implemented a representation learning approach for dimensionality reduction and identification of significant enzyme perturbations. **(B)** Experimental validation of *in silico* results through measurement of metabolic signatures (e.g. FLIM) and drug response assays. We returned to the computational model to generate additional calculations to compare to the experimentally observed metabolic imaging and drug responses, symbolizing the bidirectional arrows between panels a and b.

Materials and Methods

Constraint-based modeling

We used an existing model of central carbon metabolism, consisting of 74 reactions (including a biomass growth reaction).[21] Unsteady-state, parsimonious flux balance analysis (upFBA) was utilized to predict the distribution of fluxes for the network. This method was used due to its advantages over other methods such as traditional flux balance analysis (FBA) and unsteady-state FBA (uFBA).[21] Namely, FBA relies on the assumption of a steady-state system, where metabolite concentrations remain constant and the environment remains non-transient. However, our study focuses on investigating the impacts of different media on CRC cells in a 24-hour period; therefore, traditional FBA is not suitable for our purposes. Moreover, we have informed our model by incorporating

constraints on the metabolite fold-changes in the 24-hour period, as measured using metabolomics (previously described in Wang *et al)*.[21] While uFBA allows for the inclusion of metabolomics data and can investigate dynamical systems, we opted to use upFBA, which predicts the reaction fluxes by minimizing the total flux through the network. The decision to minimize the overall metabolic flux required for biomass production, as opposed to maximizing it as in traditional FBA or uFBA, is based on the optimality principle[29], which states that cells aim to maintain a specified growth rate while simultaneously minimizing their metabolic expenditures. By performing upFBA, we are able to predict the flux through all 74 reactions given the measured growth rate (which is set as the biomass production rate) and constraints on the metabolite fold-changes over 24 hours.

We predicted flux through the metabolic network for four conditions using this method: KRAS mutant ($KRAS^{MUT}$) and KRAS wildtype ($KRAS^{WT}$) CRC cells cultured only in CRC media or switched to CAF-CM. For notation, we use WT_{CRC} and WT_{CAF} to denote $KRAS^{WT}$CRC cells cultured only in CRC media or switched to CAF-CM, respectively. Similarly, $KRAS_{CRC}$ and $KRAS_{CAF}$ refer to $KRAS^{MUT}$ CRC cells cultured only in CRC media or switched to CAF-CM, respectively. Thus, we can compare the effects of the media or the KRAS mutation. We applied the model to simulate enzyme knockdowns, with the predicted flux distributions obtained from flux balance analysis serving as the initial reference point for introducing perturbations ("baseline model"). Gene knockdowns were performed using uFBA, as a means to predict the maximal biomass growth rate given a perturbation to the system. Thus, the constraint on biomass growth rate used above in upFBA was removed. For the full enzyme knockouts, the upper and lower bounds for each reaction's constraints were set to 0 mM/hr. For partial enzyme knockdowns, only the upper or lower bounds were changed relative to the reference flux in the baseline model without the perturbation. We use a 20% knockdown of an enzyme to illustrate our method. If the corresponding enzyme-catalyzed reaction is predicted to proceed in the forward direction in the baseline model, the upper bound would be set to 80% of the predicted flux without any perturbation. Conversely, if the reaction proceeded in the reverse direction, the lower bound would be set to 80% of the predicted flux. Therefore, this method ensures that the enzyme knockdown simulations are context-specific and considered relative to the metabolic behavior observed in the predicted flux distributions from the baseline model. All constraint-based modeling was done in MATLAB R2022a, and we utilized the COBRA toolbox v3.0. Scripts relevant to enzyme knockdown can be found on GitHub: https://github.com/FinleyLabUSC/CRC-Cell-uFBA-Modeling.

Dimensionality reduction

We leveraged representation learning for dimensionality reduction, facilitating the analysis and comparison of a large set of vectors. Representation learning employs neural networks to transform a wide range of inputs into low-dimensional features. In this work, we specifically used Siamese neural networks (SNN), which are trained on all inputs using the same network architecture.[30] As a result, the projected low-dimensional vectors can be directly compared to each other as a measure of similarity, which is our goal.

Furthermore, this approach enables comparison of the input data without the need for additional data processing, such as normalization.

We consider a vector of reaction fluxes, each 1x74 in size, for individual enzyme knockdowns. These vectors represent the predicted flux through each of the 74 metabolic reactions and signify the systemic impact of these knockdowns. Our simulation includes five levels of partial enzyme knockdowns (20%, 40%, 60%, 80%, and 100%) across four different conditions (WT_{CRC}, WT_{CAF}, $KRAS_{CRC}$, and $KRAS_{CAF}$). Consequently, we have generated a large dataset comprising 20 sets of 74x74 vectors from this metabolic modeling (1480 total perturbations). We then employ a neural network that interprets these input matrices as if they were images, with each matrix value being analogous to a pixel's intensity in an image. The network is designed to discern subtle patterns within these 'images,' especially focusing on features around the diagonal, which correspond to the enzyme knockdowns. The neural network's capability to discern subtle patterns is influenced by how the data is structured and presented. Large matrices containing all 74 knockdowns for a given condition and knockdown level are fed into the neural network, allowing it to learn from the interactions between the rows and columns of the specific input file. This is critical for creating a meaningful mapping in 2D space because the network trains on these points in the context of the larger matrices, capturing relationships within the rows and columns and optimizing the embedding space based on a complex set of features in relation to one another. This can be compared to the method by which a sophisticated car recognition system processes images of vehicles. Just as this system analyzes and learns from various visual aspects of a car (such as shape, color, etc.) to differentiate different types of cars, the neural network examines the matrices representing enzyme knockdowns as if they were intricate patterns in an image. Each 'pixel' or data point in the matrix is weighed and considered in the context of the full 'image', or the complete matrix of knockdowns, to distinguish the overarching structural features that denote similarity or dissimilarity, in the way that cars are identified in this way based on various characteristics. Through this method, the network will be able to construct a low-dimensional embedding that captures the structural features of the data, learning a representation that intrinsically captures similarities in the inputs. By computing the distance between these inputs in 2D space, we can determine the similarity between the inputs, yielding a single value that reflects the complex interrelations among the model's output features.[30] As such, the dataset is better suited for representation learning, compared to other methods.[22]

Other methods of dimensionality reduction do not produce new, learned representations of the data, but rather project the original features into low-dimensional space comprised of the original input vectors, such as in t-distributed stochastic neighbor embedding (tSNE). However, neural networks have been found in numerous previous works to reduce the dimensionality of images more effectively compared to methods such as tSNE.[31] This is in large part due to complexities within large sets of vector data that cannot be measured using predefined features. Additionally, other methods of dimensionality reduction, such as principal component analysis (PCA), are also limited in their ability to faithfully represent the data. For example, PCA fails to capture complexities in large, non-linear data sets since it only finds linear combinations of the original features.[32]

198 In our approach, the SNNs are trained on the full input set through conventional triplet
199 loss training. Note that we do not consider a test set, as we are not using the trained SNN
200 for prediction purposes. We employ this supervised form of learning because unlike
201 unsupervised learning, it can capture local and global features of high-dimensional
202 datasets.[33] As we input each vector of fluxes into the neural network, it generates a
203 corresponding triplet, which is then processed further. This triplet consists of an anchor
204 (the original data point), a positive data point (a data point in the set of inputs that is similar
205 to the anchor), and a negative data point (a data point in the set of inputs that is different
206 from the anchor). Since we are interested in understanding differences between the
207 projected data points, we calculate the Euclidean distance between points, traditionally
208 used in triplet loss. This conveys the distance between projected data as a measure of
209 dissimilarity or similarity. It is important to note that the locations of projected points are
210 influenced by the network and type of training, and therefore, the actual distances do not
211 correspond to a physical quantity. Please see Supplemental Material for justification of
212 use of Euclidean distance in the 2D space. Scripts relevant to representation learning can
213 be found on GitHub: https://github.com/FinleyLabUSC/CRC-Cell-uFBA-Modeling.

214 Cell culture conditions

215 *Maintenance.* PDTOs and CAFs were generated from CRC tumor resections received
216 from USC Norris Comprehensive Cancer Center Translational Pathology Core according
217 to Institutional Review Board (Protocol HS-06-00678) approval as outlined previously.[34,35]
218 All patients gave their informed consent before they were included in the study. PDTOs
219 and CAFs (000US - $KRAS^{MUT}$; 000UA - $KRAS^{WT}$) were grown in 5% CO_2 and 37ºC and
220 maintained in CRC media, consisting of Advanced DMEM/F-12 media (Thermofisher
221 Scientific, Waltham, MA; 12634010) and the following supplements (at their noted
222 concentrations and solvent) outlined in Table 1:

223 **Table 1:** CRC media supplements

Reagent	Solvent	Final Concentration	Vendor
Heat inactivated fetal bovine serum	N/A	10%	GeminiBio; 100-500
Penicillin : Streptomycin	N/A	5%	GeminiBio; 400-109-100
HEPES	N/A	1%	Thermofisher Scientific; 15630080
GlutaMAX	N/A	1%	Thermofisher Scientific; 35050-061
B27 supplement	N/A	2%	Thermofisher Scientific; 17504-001
N2 supplement	N/A	1%	Thermofisher Scientific; 17502048

N-acetylcysteine	Water	1 mM	Sigma Aldrich, A9165
Nicotinamide	Water	10 mM	Sigma Aldrich, N0636
Noggin	0.1% BSA in PBS	100 ng/mL	Peprotech, 120-10C
EGF	1% BSA in PBS	50 ng/mL	Thermofisher Scientific; PHG0313
SB202190	DMSO	10 μM	Sigma Aldrich, S7067
A-83-01	DMSO	500 nM	Millipore, 616454-2MG

224 PDTOs were maintained by embedding in Cultrex Reduced Growth Factor Basement
225 Membrane Extract, Type 2 (BME; R&D Systems, Minneapolis, MN; 3533-001-02) and
226 droplets of 60μL were plated onto 24-well plates. The plates were allowed to slightly gel
227 at room temperature for 1 minute before flipping over and placed into the incubator for 15
228 additional minutes for full gelling. CRC media was then gently added to the wells to
229 maintain the cultures.

230 *Assay set-up.* PDTOs were dissociated into single cells when prepared for imaging and
231 CellTiter-Glo (CTG; Promega, Madison, WI, G9681) cell viability assays. 500 μL Gentle
232 Cell Dissociation Reagent (STEMCELL Technology, Cambridge, MA; 07174) was added
233 to each well, followed by scraping of the organoid/BME droplets with a P1000 pipette tip.
234 This cell suspension was then rocked at 4ºC for 30-35 mins in a 15 ml conical tube.
235 Organoid suspensions were centrifuged at 300x*g* for 5 minutes and the BME/dissociation
236 reagent was carefully removed. A 1:1 fragmentation solution of 1X DPBS and TrypLE
237 (Thermofisher Scientific, Waltham, MA; 12605028) plus 1:1000 ROCK inhibitor, Y-27632
238 (STEMCELL Technology, Cambridge, MA; 72302) was used to resuspend the cell pellet
239 and allowed to incubate at 37ºC for 1-2 minutes with physical agitation every 30 seconds.
240 Periodic checks of the cell suspension were done under a microscope to ensure that a
241 majority of the organoids were fragmented. After confirmation that most organoids were
242 dissociated to single cells, the fragmentation solution was quenched by adding 2X volume
243 of CRC media to the cell suspension. The cells were then centrifuged at 300x*g* for 5
244 minutes and resuspended in CRC media. The single-cell suspension was passed through
245 a 40 μm cell strainer to remove larger organoid fragments. Live cell counts were
246 measured using the TC20 automatic cell counter (Bio-Rad, Hercules, CA). The required
247 amount of cells/assay were suspended in BME with 10% collagen I (Sigma Aldrich, St.
248 Louis, MO; C3867, stock concentration 2.5 mg/mL) to a concentration of 100,000
249 cells/mL. 10 μL of the cell suspension was plated as a droplet to each well of a white-wall
250 clear-bottom 96-well plate (Corning, Glendale, AZ; 3903) for CTG assays or a clear-
251 walled glass-bottom plate (Mattek, Ashland, MA; P96G-1.5-5-F) for FLIM imaging. Plates
252 were incubated for 10 minutes at 37ºC inverted. 200 μL of CRC media containing 1:1000
253 ROCK inhibitor Y-27632 (STEMCELL Technology, Cambridge, MA; 72302) was then
254 added to each well to maintain the organoids until drug treatments were initiated.

255 *Conditioned media.* CAF conditioned media (CAF-CM) was generated when patient
256 derived CAFs were grown in 10 cm^2 tissue culture dishes to about 70-80% confluency in
257 CRC media. Media was refreshed with new CRC media and allowed to be conditioned by
258 the CAFs for 72 hours before collection and filtering through a 40 µm pore size filter.
259 Collected media was stored at -30ºC until assay use.

260 Drug treatments and cell viability assays

261 Various concentrations of staurosporine (STA; Sigma-Aldrich, St. Louis, MO; 569396), 5-
262 fluorouracil (5-FU; Selleck Chemicals, S1209), 7-ethyl-10-hydroxycamtothecin (SN-38;
263 Sigma-Aldrich, St. Louis, MO; H0165), or 3-bromopyruvate (3-BP; Sigma-Aldrich, St.
264 Louis, MO; 16490) were added to their respective wells. For plates reserved for FLIM
265 imaging, DRAQ-7 (Abcam, Cambridge, MA; ab109202) was added to each well at a final
266 concentration of 3 µM. Control samples to demonstrate metabolic inhibition were treated
267 with 100 mM sodium dichloroacetate (Sigma-Aldrich, St. Louis, MO; 347795) and 50 mM
268 2-deoxyglucose (Sigma-Aldrich, St. Louis, MO; D6134) for 24 hours prior to FLIM
269 imaging.

270 For cell viability assays, PDTOs were cultured for 4 days in CRC media before the
271 addition of any drugs, as described above. After 5 days of treatment, CTG assays were
272 conducted as described by the manufacturer. For FLIM experiments, organoids were
273 grown for 7 days and then treated with drugs for 6 or 72 hours prior to imaging.

274 Fluorescence lifetime imaging microscopy (FLIM) and data analysis

275 FLIM imaging was done at the Translational Imaging Center (TIC) at the University of
276 Southern California (USC) and at the Ellison Institute of Technology (EIT). For images
277 taken at the TIC, a Zeiss 780 inverted confocal microscope (Carl Zeiss, Jena, Germany)
278 was used. 256x256 pixel sized images that were taken with a Plan-Apochromat M27
279 20X/0.8 NA (Carl Zeiss, Jena, Germany) objective at 12.6 µs pixel dwell time. The PDTO
280 samples were excited with a Ti:Sapphire 2-photon laser (Coherent Chameleon Ultra II)
281 set at 740 nm for NAD(P)H excitation. The emission was split into two channels with a
282 590 nm long-pass filter and each channel was further filtered at 460/80 nm for NAD(P)H.
283 External photomultiplier tube detectors (Hamamatsu, Japan R10467U-40) were used to
284 detect the emission for each channel. An A320 FastFLIM FLIMbox (ISS Inc., Champaign,
285 IL.) was used to collect the frequency domain lifetime of NAD(P)H with VistaVision
286 software (ISS Inc., Champaign, IL). An averaging of 4 frames per z-slice was done to
287 collect enough photons for FLIM analysis. For confocal images on the Zeiss 780, 512x512
288 images were taken with a 633 nm excitation for DRAQ7.

289 FLIM imaging performed at EIT was done on an Olympus FV3000 microscope with a
290 UPLXAPO 20X/0.8NA objective, which was upgraded with an A320 FastFLIM FLIMbox
291 (ISS Inc., Champaign, IL.) add-on and hybrid PMT external detectors (Hamamatsu,
292 Shizuoka, Japan). Samples were excited at 740 nm with a Ti:Sapphire 2-photon laser
293 (Spectra-Physics, Mountain View, CA) at 15-20 mW and the emission was passed
294 through a 458/64 dichroic for NAD(P)H collection. VistaVision software (ISS Inc.,
295 Champaign, IL) was used to collect the data. 256x256 images were taken with a pixel

296 dwell time of 10 μs/pixel. An averaging of 10 frames per z-slice was done to collect
297 enough photons for FLIM analysis. 512x512 confocal images for DRAQ7 vital dye staining
298 were taken with 640 nm excitation.

299 Both systems were calibrated in a similar fashion with a solution of coumarin-6 in 200
300 proof ethanol (known lifetime of 2.5 ns). Collection of the FLIM data was done until the
301 average photon count was about 100 counts/pixel. Organoids of 100-120 μm were
302 manually selected for imaging to ensure that oxygen diffusion limits were not a
303 contributing factor. Three z-slices of each organoid were taken, where the middle slice of
304 the z-stack was the center of the organoid. Image files were exported as .R64 files through
305 VistaVision and analyzed with SimFCS software (Laboratory for Fluorescence Dynamics,
306 University of California, Irvine).

307 Hexokinase (HK) activity assay

308 Dissociated PDTO single cells were mixed with BME and seeded in a 24-well plate at
309 200,000 cells/mL. 60 uL of the BME cell suspension were seeded in each well and
310 incubated inverted at 37ºC for 10 mins to allow for BME gelling. Organoids were grown
311 for 7 days in CRC media before being treated with CRC media or CAF-CM spiked with 3-
312 BP. After treatment for 24 hours, organoids were digested with a gentle dissociation buffer
313 and rocked for 40 minutes at 4ºC. Cells were collected by centrifugation at 300x*g* for 5
314 minutes. BCA protein assay (Thermofisher Scientific, Waltham, MA; 23225) was
315 conducted to normalize protein concentrations between all samples and hexokinase
316 activity was measured according to the manufacturer's protocol (Abcam, Cambridge, MA;
317 ab136957), using 10 μg of protein per condition. Readings were collected on a Biotek
318 Synergy Neo2 plate reader (Agilent, Santa Clara, CA) every 5 minutes for 3 hours to
319 capture the window of optimal reaction readings for initial and final time points.

320 Statistical analysis

321 Statistical analysis was performed using R in the RStudio environment.[36]

322 For FLIM imaging, fraction bound was calculated for three Z-slices of each organoid, then
323 averaged together to produce one summary fraction bound value for each organoid. To
324 account for the variation between organoids within each well we used a mixed effect
325 model constructed with the lmer() function from version 1.1-35.1 of the lme R[38] package.
326 We constructed mixed effect models for each test drug with an interaction term for drug
327 dose and media type to examine how the effects of each drug changed when adding
328 CAFs.

329 To examine the action of the drugs at individual doses, we corrected for differences
330 between experiments with batchma's adjust() function,[37] checked normality using the
331 check_normality function from the performance package, and conducted an ANOVA test
332 using stats's aov() to compare the fraction bound between doses of 3-BP for CAF and
333 CRC media types.

334 Data from cell viability CTG experiments were used to construct dose response curves
335 (DRCs) for all experimental conditions. Drug conditions were normalized to within-plate

negative control (untreated) wells and positive control wells (STA treated). These controls were used to calculate percent relative viability using the following formula:

$$Drug\ condition\ \%\ relative\ viability\ = \frac{drug\ mean\ RLU\ -\ STA\ mean\ RLU}{untreated\ mean\ RLU\ -\ STA\ mean\ RLU} \times 100$$

Where drug mean RLU corresponds to the mean relative luminescence units (RLU) over six technical replicate wells in a single plate. STA mean RLU corresponds to the mean RLU of the six technical replicate wells of STA; and untreated mean RLU corresponds to the mean RLU of the six technical replicated wells of the untreated condition. Individual wells were submitted to image QC and excluded if microscopy images showed evidence of debris or poor plating.

The drug condition % relative viability results from a single plate were examined together and used to model a DRC using R Studio[38]. The *logistic()* function from version 3.0.1 of the *drc*[39] R[36] package was used to determine which log-logistic regression model fit each curve. Most compounds produced a four-parameter curve, which were subsequently produced (after model selection) using the *LL.4()* function from the same version of drc. SN-38, however, produced a five-parameter asymmetric curve in all biological replicates. Dose response curves for SN-38 were subsequently formulated using *logistic()*.

After modeling the DRCs for each biological replicate, we evaluated them using several quality control (QC) criteria **(Supplementary Table 1**). We calculated Z'Factor[40] for each biological replicate and used only experiments where this statistic was greater than 0 to ensure that a sufficient window between positive and negative controls existed to accurately examine differences in RLU between drug conditions. We calculated plate CV_{avg}[41] using the following formula:

$$\text{plate } CV_{avg.}\ =\ average(condition\ CV_{avg.})\ ,$$

where

$$condition\ CV_{avg.}\ =\ sd(signal)/average(signal)x100$$

for each compound and concentration.

Iverson *et. al.*[41] recommends a bound of 20% for homogeneous cell line assays, but PDTOs displayed a more variable signal by condition, so we used a bound of 30%. Absolute IC_{50}s were used to compare potency between conditions, so biological replicates with extrapolated IC_{50}s were considered to fail quality control criteria. Residual standard error (RSE) was calculated by the *drm*() function from version 3.0.1 of the drc R package. We used a bound of RSE < 20 to eliminate dose response models that may have been made less accurate by residuals. Finally, models with an upper asymptote 95% confidence interval below 55% relative viability were eliminated to ensure that we only examined models with an upper asymptote that is closer to 100% relative viability.

While only biological replicates that passed the above quality control criteria were considered for official analysis, we ensured that the results were the same when all

biological replicates were considered. See **Supplementary Table S1** for summary of QC metrics and number of runs for each condition which passed QC. Absolute IC_{50} means were significantly different between replicates cultured with and without CAF-CM when considering all replicates using Welch's *t*-test (*p*-value = 0.020). When using all replicates, excluding those that did not pass QC criteria, absolute IC_{50}s were found to be significantly different using the same test (*p*-value = 0.007).

Scripts for statistical analysis are available on GitHub at: https://github.com/FinleyLabUSC/CRC-Cell-uFBA-Modeling.

Results

Constraint-based modeling of CRC central carbon metabolism predicts the distribution of fluxes for distinct growth changes.

We used an existing model of the metabolic pathways in central carbon metabolism from Wang *et al.*[42] to investigate the metabolic crosstalk between CRC cells and CAFs. As detailed in that study, unsteady-state parsimonious flux balance analysis is used to determine the flux for each reaction in the model of central carbon metabolism, given mass balance constraints and measured fold-changes from metabolomics data.[42] We predicted flux through the metabolic network for four conditions: WT_{CRC}, WT_{CAF}, $KRAS_{CRC}$, and $KRAS_{CAF}$, as described in the methods. We utilized the same metabolomics constraints and pre-defined growth rates as in our prior work.[21] The predicted fluxes for $KRAS^{MUT}$ cells considering the effect of the growth media are distinctly shown in **Supplementary Figure S1**. These results are the focus of this work, given the prevalence of colorectal cancers with the KRAS mutation and the overall worse prognosis; however, for completeness, predictions to investigate the effect of growth media and gene mutation are shown in **Supplementary Figures S2 – S4.** For the remainder of this work, we focus on $KRAS^{MUT}$ cells in the two media types. The predicted flux distributions for $KRAS^{MUT}$ cells were then used as an initial point for performing a wide set of enzyme knockdowns in the network and serve as the "baseline" points in our study, where there is no perturbation.

Heatmap visualization of enzyme knockdowns in central carbon metabolism unveils widespread effects and dynamic responses.

In addition to understanding the predicted flux distributions for the various conditions, we simulated perturbations to investigate the network-wide responses to enzyme knockouts. We aimed to expand the efforts of Wang *et al*[21], whose work concentrated solely on the effects of complete enzyme knockouts on the biomass reaction. It is common to study how biomass is affected by metabolic perturbations; however, this approach does not produce a broader understanding of the network-level response to alterations. Therefore, we fully inhibited the activity of each enzyme within the network and looked at its resultant impact on overall network functionality. We further developed this analysis to include

partial enzyme knockdowns (at levels of 20%, 40%, 60%, and 80%) across the entire network.

We summarize and display the impact of 100% enzyme knockdowns for $KRAS_{CAF}$ specifically in the heatmap shown in **Figure 2**. Each row corresponds to a single enzyme knockdown in the network, while the columns correspond to the predicted fluxes of reactions for the given enzyme knockdown. Each box corresponds to a single flux value. The heatmap view allows us to examine flux changes after metabolic perturbations at the network level. We show all generated heatmaps for each condition and partial knockdown in **Supplementary Figure S5A-D**.

In several instances, we see that the predicted fluxes are independent of which enzyme is inhibited, as indicated by the same colors extending vertically down the figure. For example, the figure shows that, overall, metabolic perturbations in multiple pathways lead to an increase in glycolytic flux, as indicated by the red hue extending vertically within the block of glycolysis reactions on the left side of the figure. Most metabolic perturbations cause a decrease in flux through transport and exchange reactions, represented by a blue hue that extends vertically on the right side of the figure. Additionally, following knockdown of almost any enzyme in the network, certain enzymes such as isocitrate dehydrogenase (IDH 2/3), fumarate hydratase (FUM 2/3), malate dehydrogenase (MDH 1/2), and glutamate dehydrogenase (GDH 1/2/3) are predicted to exhibit either very high or low flux values near the boundary points, 500 and -500 respectively.

Upon closer inspection, certain knockdowns cause unique effects within the network that are not seen in response to other metabolic perturbations. For instance, in glycolysis, the knockdown of lactate dehydrogenase (LDH) causes a significant reduction in the activity of phosphoglycerate kinase (PGK) relative to other enzymes inhibited in the glycolytic pathway. This reduction shifts the metabolic flow away from the normal PGK pathway, resulting in an increase in the Rapoport-Luebering shunt activity within glycolysis, shown by the increased flux through both diphosphoglycerate mutase (DPGM) and diphosphoglycerate phosphatase (DPGase). Another example is the effect of inhibiting glyceraldehyde-3-dehydrogenase (GAPDH), which leads to a reduced flux through DPGM and therefore DPGase. Inhibiting LDH also leads to an enhanced positive flux in the initial reactions of the TCA cycle. Further analysis indicates that these types of unique effects can be found within pathways other than just glycolysis. Contrarily, there may appear to be similarities in effects across these knockdowns; biologically, this could suggest a certain level of redundancy and robustness in the metabolic pathways. However, these differential effects are difficult to decipher efficiently by solely analyzing the heatmap. Therefore, we sought to develop an alternate strategy for identifying effective metabolic perturbations.

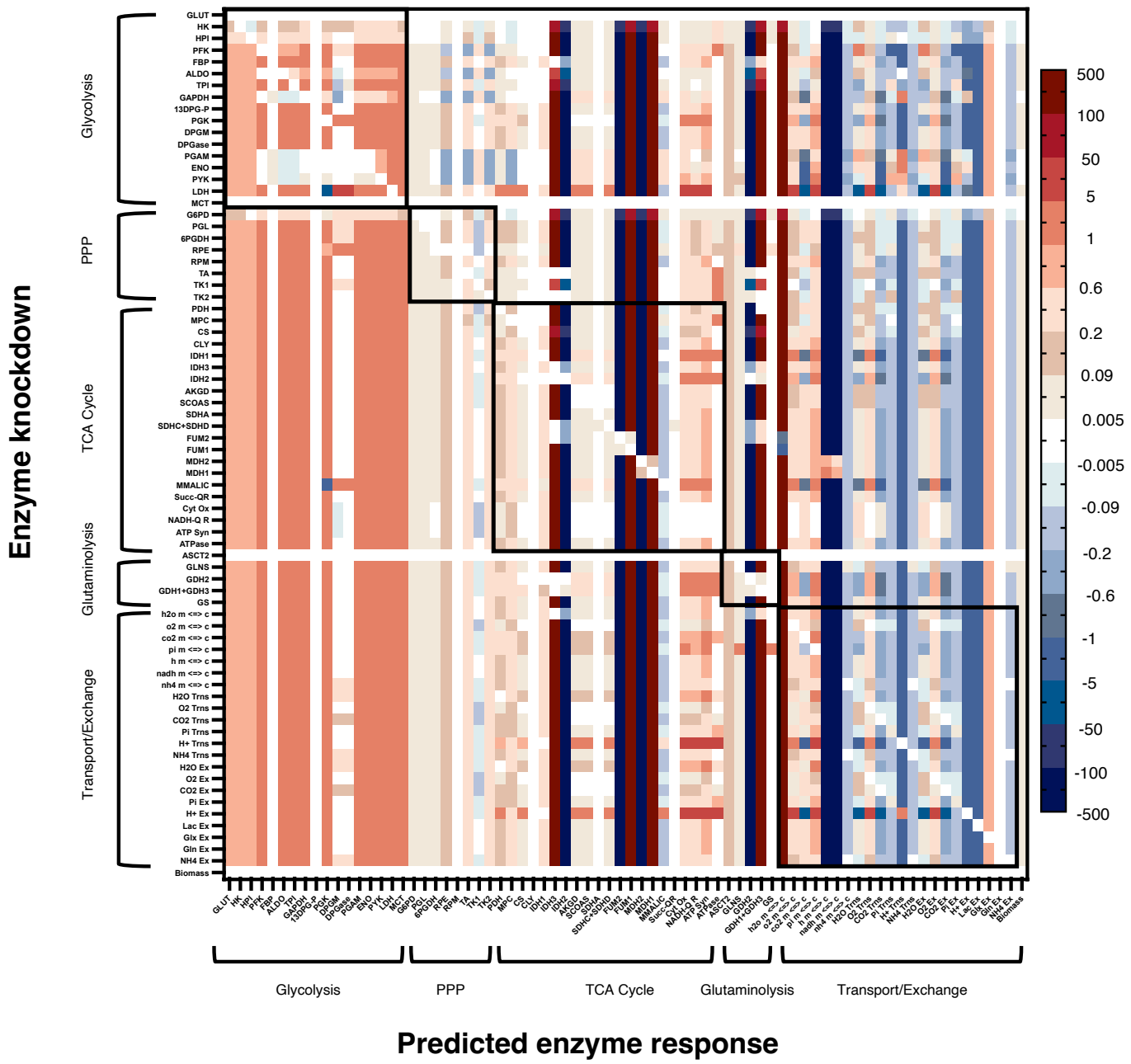

Figure 2: Heatmap displaying the impact of complete (100%) enzyme knockouts on absolute reaction fluxes for the $KRAS_{CAF}$ condition. Rows represent individual enzyme knockdowns, while columns depict the effects of each perturbation on the rest of the network (predicted enzyme response). The color axis represents the absolute flux of enzymes following perturbations. Intensifying red shades signify positive flux values, while progressively deeper blues correspond to negative flux values. White fluxes signify values either equal to zero or close to zero. The outlined boxes represent the self-regulatory effects of knockdowns within individual central carbon metabolism pathway.

Dimensionality reduction helps visualization and comparison of the effects of the metabolic perturbations.

As denoted in **Figure 2,** heat maps can be used to visualize the network-level responses to inhibiting individual metabolic enzymes. However, it is difficult to compare across the conditions and perturbations, given the number of enzyme knockdowns simulated for each condition and the wide range of predicted flux values. Thus, we considered an alternative way to represent and visualize the predicted fluxes. We utilized a machine learning approach to perform dimensionality reduction and cast the distribution of fluxes within the network, considering enzyme knockdowns, into a 2D projection space (**Figure 3A**). This approach makes use of neural networks to reduce the dimensionality of model outputs and then to calculate the distance between the projected points to determine how different they are from each other.[30] Plotting the predicted reaction fluxes in 2D space is a vast reduction in the dimensionality of the model output, as each point represents the flux through all 74 reactions in response to a single enzyme knockdown. **Figure 3A** displays 1480 points (termed "coordinates") in 2D space, derived from 4 conditions (WT_{CRC}, WT_{CAF}, $KRAS_{CRC}$, and $KRAS_{CAF}$), 74 enzyme knockdowns, and 5 different levels of inhibition. Each coordinate represents a single simulation, denoting a specific knockdown and its subsequent impact on the metabolic network, representing a row of the heatmap in **Figure 2**. The points denoted in red correspond to the calculated centroid (the "average" of all points for each condition).

When the simulation coordinates are labeled according to their respective condition, they create distinct clusters, implying significant differences among the four conditions and reinforcing each condition's uniqueness. We can infer the similarity of the predicted flux distributions based on how close the points are in the 2D projection space. While we cannot necessarily assign biological meaning to the two dimensions, based on the neural network training, the distance between points is a metric to represent their similarity (see Methods section for details). Thus, the grouping together of points in each condition indicates that they share similar characteristics. The two CAF-CM conditions (in darker colors) show more separation compared to the two CRC media conditions (in lighter colors). The coordinates corresponding to the $KRAS_{CAF}$ condition are distinctly isolated from the rest of the simulation coordinates. We considered alternative dimensionality reduction methods, including t-distributed stochastic neighbor embedding (t-SNE) and uniform manifold approximation and projection (UMAP) (**Supplementary Figure S6**); however, these methods do not recover the distinct grouping of the four conditions simulated and cannot be used to compare the effects of the metabolic perturbations. We note that the t-SNE and UMAP utilize unsupervised learning methods, and cannot correctly cluster the complex, non-linear data generated by the gene knockdowns. In contrast, the dimensionality reduction method is a supervised learning approach using representation learning, in which the simulated gene knockdowns are fed into the neural network as labeled inputs representing four conditions. Thus, it is not surprising that our approach shows clustering of points within the four conditions. Our primary purpose of using representation learning is to identify metabolic perturbations that produce significantly altered flux distributions, rather than clustering, and we describe the steps to determine influential perturbations.

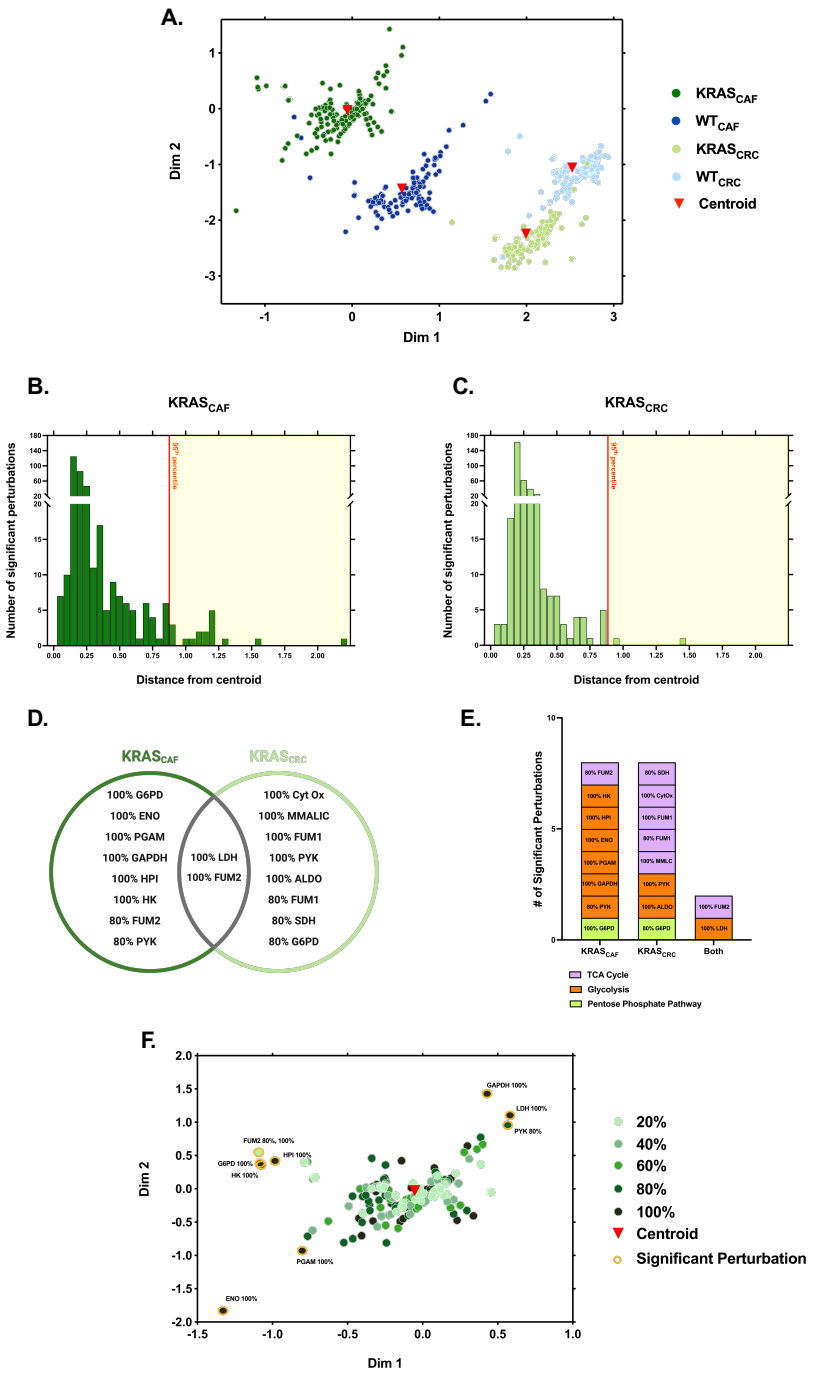

Figure 3: Dimensionality reduction and data analysis. (A) Predicted reaction fluxes due to metabolic perturbations projected in 2D space. **(B-C)** Distributions of distances between each simulation point in 2D space to its cluster centroid for $KRAS_{CAF}$ and $KRAS_{CRC}$ respectively. **(D)** Influential metabolic perturbations identified for $KRAS_{CAF}$ and $KRAS_{CRC}$, respectively. **(E)** Characterization of identified reactions of significance for $KRAS_{CAF}$ and $KRAS_{CRC}$ according to central carbon metabolism pathways. **(F)** Labeling of simulated perturbations and identification of significant reactions in $KRAS_{CAF}$ 2D Projection Space.

Identification, classification, and analysis of influential perturbations for $KRAS_{CAF}$ and $KRAS_{CRC}$.

Next, we sought to identify significant metabolic perturbations of interest by examining the distributions of the Euclidean distances between each perturbed simulation coordinate and the calculated centroid for each condition. The distance between points in the projection space can be used to identify enzyme knockdowns that drastically shift the flux distribution from the base state (**Figure 3B-C** and **Supplementary Figure S7A-B**). Our objective is to pinpoint perturbations that notably influence reaction flux values. We focus on the perturbations for $KRAS^{MUT}$ cells, due to its clinical significance, and we consider the effect of CAF-CM due to the evidence in literature that CRC-CAF interactions promote drug resistance.[43,44] We note that inputs to the SNN must have the same dimensions. As described in the Methods section, we trained the SNN to learn 2D representations of 74x74 matrices containing the predicted flux through each of the 74 reactions in our metabolic model when each of the 74 metabolic enzymes is perturbed. The baseline reaction flux vector is 1x74, and hence, cannot be inputted into the SNN since it is of a different dimension. Therefore, we consider the centroid of a cluster when identifying influential perturbations. Thus, we computed the Euclidean distances in the 2D learned space between the cluster centroid and each coordinate pertaining to $KRAS_{CAF}$ and $KRAS_{CRC}$ conditions and constructed separate histograms for each condition to study the distribution of these distances. For both conditions, the distances between the simulation coordinate and the centroid due to a metabolic perturbation fall between 0 and 0.5 (**Figure 3B-C**), indicating that the majority of perturbations produce network fluxes whose coordinate in the learned 2D space lie close to the centroid. Since all histograms presented as right-tailed distributions, we represented significant perturbations as the simulation coordinates that lie at the furthest end of the tail, which captures the most extreme deviations in each condition. Specifically, we use distances within the 95th percentile for $KRAS_{CAF}$ and $KRAS_{CRC,}$ indicating the top 5% of coordinates with distances furthest from the centroid. From these subsets (19 influential perturbations for $KRAS_{CAF}$ and 37 for $KRAS_{CRC}$), we selected the perturbations that correspond to the top 10 distances for a detailed comparison. This selection process allowed us to effectively examine the impact of different growth conditions, illustrated in **Figure 3D**.

We classified the influential perturbations based on their metabolic pathway for both conditions, which revealed distinct differences for $KRAS_{CAF}$ and $KRAS_{CRC}$ (**Figure 3E**). The top 10 perturbations for $KRAS_{CAF}$ primarily target glycolytic reactions, while those for $KRAS_{CRC}$ inhibit TCA cycle reactions. Importantly, the influential perturbations identified by our selection process for the $KRAS_{CAF}$ condition include fully inhibited HK and glucose-6-phosphate dehydrogenase (G6PD), which were found to be reactions of importance in the work of Wang *et al*. as well.[42] Among the top 10 most influential perturbations for $KRAS_{CRC}$, two reactions from glycolysis were identified: fully inhibited pyruvate kinase (PYK) and aldolase (ALDO). Interestingly, these reactions represent the downstream reactions of glycolysis, in contrast to $KRAS_{CAF}$, where inhibiting the initial reactions most strongly alters the flux distribution. Additionally, while G6PD is shown to be a significant perturbation in both conditions, inhibiting the enzyme by 80% produces a large shift in the predicted fluxes for the $KRAS_{CRC}$ condition, as opposed to a 100% knockdown eliciting a

554 large shift in the flux for the $KRAS_{CAF}$ condition. Thus, CAF-conditioned media is predicted
555 to make CRC cells more robust to perturbations. Furthermore, completely inhibiting LDH
556 and FUM2 are shown to be influential perturbations for both the $KRAS_{CAF}$ and $KRAS_{CRC}$
557 conditions, revealing examples of enzyme knockdowns that can alter network flux,
558 regardless of the cell's growth media.

559 We can also gain insights into how similarly the top 10 metabolic perturbations are
560 predicted to affect the flux distributions by considering their coordinates in the 2D
561 projection space. To directly pinpoint where each of the significant perturbations fall in
562 relation to one another, we labeled them on the scatterplot of 2D projections of enzyme
563 knockdowns. We focus on the $KRAS_{CAF}$ condition (**Figure 3F**). This analysis provides
564 insight into the similarities in flux distributions in response to the metabolic perturbations
565 predicted to be most influential. For instance, the coordinates for GAPDH, LDH, and PYK
566 knockouts are positioned close together in one area of the projection space, whereas
567 FUM2, G6PD, HK, and hexose phosphate isomerase (HPI) are closer to each other on
568 the end of the plot. The knockouts of enolase (ENO) and phosphoglycerate mutase
569 (PGAM) exhibit distinct activities that set them apart from the rest. Furthermore, color-
570 coding the points based on the strength of the knockdown indicates that the points farthest
571 from the centroid do not exclusively correspond to complete enzyme inhibitions.
572 Dimensionality reduction reveals that the total inhibition of a non-influential enzyme
573 results in a position near the cluster centroid, which suggests that it closely resembles
574 other perturbations with minimal system impact.

575 The significant perturbations for $KRAS_{CAF}$ produce diverse metabolic 576 changes on the network using various mechanisms.

577 The coordinates of the flux distributions given specific metabolic perturbations in 2D
578 projection space, and their distances from the centroid, indicate the effect of a
579 perturbation at the network level. We can further investigate the effects of metabolic
580 perturbations on biomass production (a proxy for growth) and at the pathway level. We
581 particularly focus on the $KRAS_{CAF}$ condition and consider how flux through glycolysis,
582 TCA cycle, the PPP, and glutaminolysis is altered.

583 Based on our analysis of the metabolic perturbations in 2D projection space (**Figure 3**),
584 we studied the effect of complete knockout of the HK reaction, an influential perturbation
585 identified in our analysis, for the $KRAS_{CAF}$ condition. Previous work *in silico* has shown
586 that HK could be a vulnerable enzyme target to disrupt the crosstalk between CRC cells
587 and CAFs.[10] Thus, we aim to further investigate how inhibition of HK could affect different
588 metabolic pathways within CRC cells. Such mechanistic understanding could be
589 leveraged to improve clinical outcomes. We compared HK knockdown to both the
590 baseline condition (with no perturbation) and to the knockdowns whose coordinates are
591 in the left-most tail of the distribution of distances (bottom 5th percentile). We consider
592 those perturbations as "reference" points, as they are not predicted to significantly alter
593 the baseline flux distribution due to their proximity to the centroid in the 2D projection
594 space. Lastly, we also considered the effect of completely inhibiting cytochrome oxidase

595 (CytOx), a metabolic perturbation identified to specifically alter network flux for the
596 $KRAS_{CRC}$ condition, but not for the $KRAS_{CAF}$ condition.

597 We found that the knockout of HK effectively inhibits glycolysis, consistently yielding
598 reduced fluxes, compared to both baseline and reference points. **(Figure 4A).** On
599 average, the knockdown of HK resulted in an 88% reduction in the fluxes through
600 glycolytic reactions compared to baseline. Furthermore, HK shutdown produces a
601 reduced flux of 0.271 hr^{-1} through LDH compared to 2.01 hr^{-1} in the baseline condition.
602 Therefore, less lactate is produced and secreted from the cell. In the PPP, a distinct
603 decoupling is observed between the oxidative and non-oxidative arms **(Figure 4B)**. The
604 knockout of HK significantly reduces fluxes in the non-oxidative arm of the PPP, with a
605 flux sum of -0.001 hr^{-1}, compared to baseline and the mean of the reference points (0.257
606 hr^{-1} and 0.192 $hr^{-1,}$ respectively). In contrast, knockout of HK increases the flux in the
607 oxidative arm of the PPP, with a flux sum of 0.170 hr^{-1}, but is still less than baseline and
608 mean of reference points (0.577 hr^{-1} and 0.455 hr^{-1}). In addition, there is substantial
609 inhibition of the TCA cycle when HK is knocked out, compared to the baseline and the
610 reference conditions (**Figure 4C**). The baseline and mean of reference points resulted in
611 a flux sum of 0.867 hr^{-1} and 0.504 hr^{-1} respectively, while HK knockout resulted in a sum
612 of 0.0353 hr^{-1}. Overall, the knockout of CytOx produced similar fluxes compared to
613 baseline for glycolysis, PPP, and the TCA cycle. Lastly, the perturbations change flux
614 through glutaminolysis reactions in various ways (**Figure 4D**). With knockouts of HK,
615 GDH2 fluxes increase notably from the baseline value of -0.423 hr^{-1} to 0.007 hr^{-1}. A
616 negative flux means that the cells produce glutamate from α-ketoglutarate, while a
617 positive flux means glutamate is being used to produce α-ketoglutarate. Thus, the model
618 predictions primarily suggest a significant accumulation of glutamate in the cell.
619 Interestingly, the median value of the reference points was even higher at 0.0486 hr^{-1},
620 aligning with the point made in **Figure 2** that GDHII is a sensitive enzyme, vulnerable to
621 a number of metabolic perturbations in the network. Knockout of HK increases the flux
622 through the glutamine synthetase (GS) reaction, from a baseline of 0.00145 hr^{-1} to 0.0316
623 hr^{-1}, indicating an upregulation of glutamate conversion to glutamine within the cell. The
624 average of reference points corresponds to a flux sum of 0 hr^{-1}, suggesting that GS is
625 also a sensitive reaction in the network, where a full knockout of any enzyme results in
626 very little flux through this reaction. The flux for glutaminase (GLNS) is nearly identical for
627 baseline and mean reference points (0.0710 hr^{-1} and 0.0732 hr^{-1}, respectively) but is
628 slightly decreased when HK is knocked out (0.0417 hr^{-1}), suggesting less glutamine
629 consumption since there is an accumulation of glutamate.

630 In summary, we have systematically inhibited metabolic enzymes in a computational
631 model of central carbon metabolism that accounts for metabolic crosstalk between CRC
632 cells and CAFs. We evaluated how the metabolic perturbations affect flux through the
633 network and identified which enzymes should be inhibited to significantly alter the network
634 flux using a machine learning approach. This work provides a novel method of screening
635 potential metabolic perturbations. We next sought to confirm our *in-silico* findings
636 experimentally.

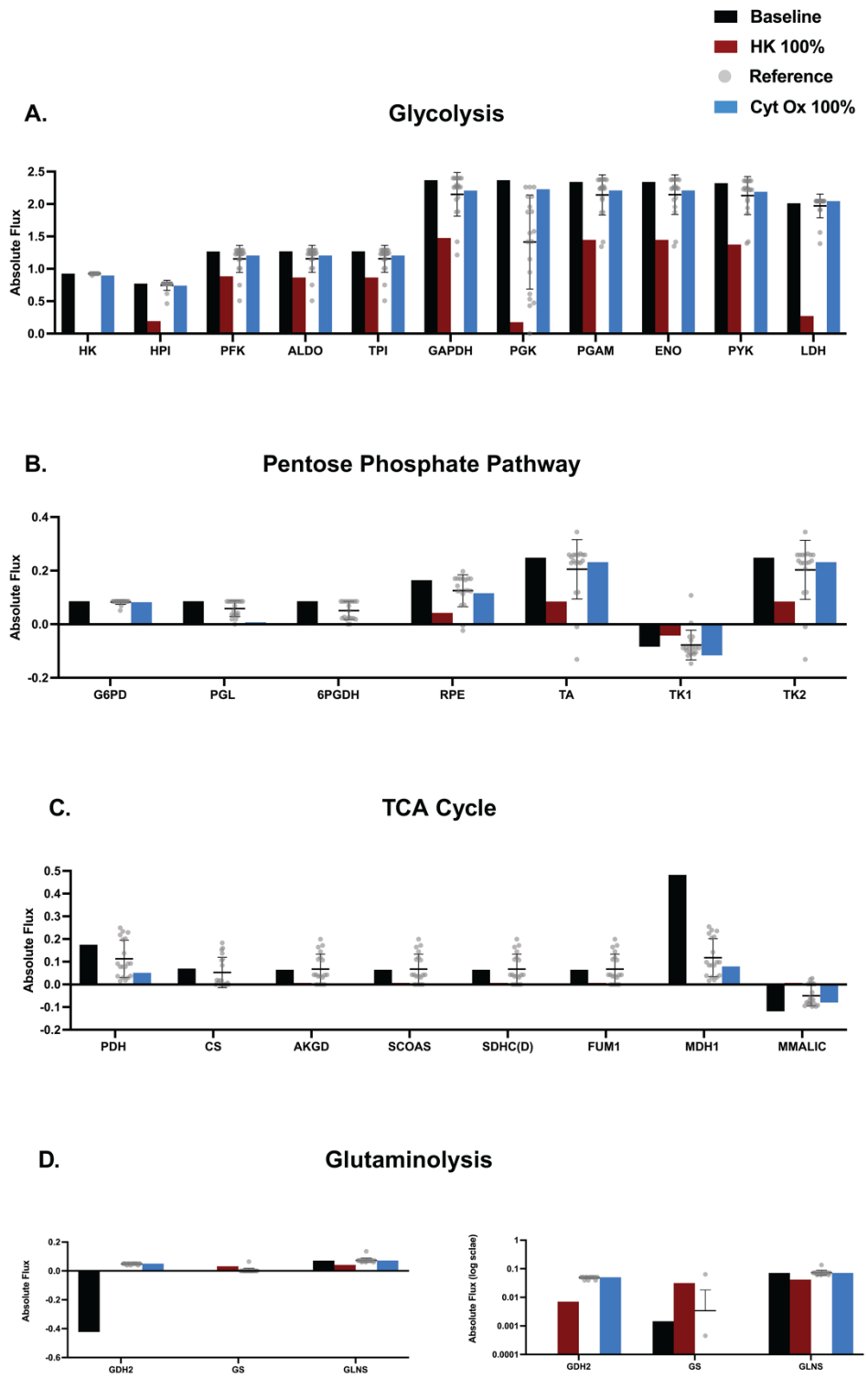

Figure 4: Comparative analysis of the impact of significant perturbations on metabolic pathways for the $KRAS_{CAF}$ condition. Bar plots depicting the fluxes for baseline (no perturbation), HK 100% knockdown, and reference (bottom 5th percentile of reactions furthest from the centroid) for reactions in **(A)** glycolysis, **(B)** PPP, **(C)** TCA cycle, and **(D)** glutaminolysis. The effects of inhibiting CytOx, a perturbation found to strongly alter network flux for the $KRAS_{CRC}$ condition, were also examined.

Pharmacological HK inhibition reduces HK activity in KRAS^{MUT} PDTOs cultured in CAF-CM.

Given HK is an enzyme of interest, we investigated whether experimental inhibition would correlate with our *in-silico* results. While the metabolic model includes the general form of the HK enzyme, we focused on inhibiting hexokinase 2 (HK2) using 3-bromopyruvate (3-BP), as it has been shown to be a predictor of patient prognosis.[45–48] HK2 is used as the isoform experimentally due to specific regulatory and kinetic properties that is applicable for studies on cancer metabolism, while the computational model simplifies the HK reaction to a more generic step in glycolysis.[49] KRAS^{MUT} PDTOs were treated with 50 and 100μM of 3-BP in CRC media or CAF-CM generated from autologous CAFs. Hexokinase activity was measured after 24 hours of treatment with 3-BP to confirm inhibition (**Figure 5**). Results showed a significant reduction of HK activity to 28.4% in PDTOs cultured in 100μM 3-BP spiked CAF-CM only.

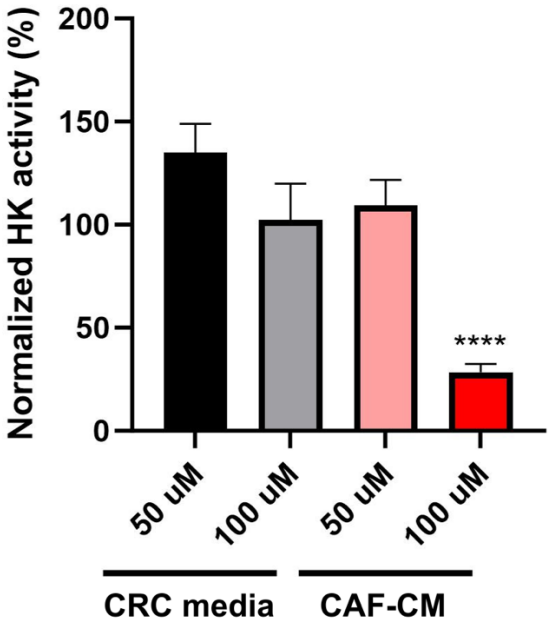

Figure 5: Hexokinase activity in PDTOs treated with 3-BP inhibitor. KRAS^{MUT} PDTOs (000US) treated with 3-BP for 24 hours in CRC media and CAF-CM to measure inhibition of HK activity. Percentage of HK activity is normalized to the respective untreated conditions (CRC or CAF-CM media). ****p<0.001

HK inhibition alters metabolic activity and cell viability in PDTOs cultured in CAF-CM.

FLIM has been a widely used imaging platform to measure metabolic signatures and drug responses within biological samples;[50–56] however, to a lesser degree in PDTOs given the recent adoption of this model system in cancer research and the complex 3D structures. The fluorescent lifetime of NAD(P)H was measured within our PDTOs, and phasor analysis was performed by taking the Fourier transform of the fluorescence emission of each pixel of the image.[26,57] We measured changes in metabolic signatures and quantified the fraction of bound NAD(P)H. An increased fraction bound of NAD(P)H

671 corresponds to a metabolic shift towards oxidative phosphorylation (OXPHOS) and a
672 decrease of fraction bound of NAD(P)H is indicative of a shift towards glycolysis
673 (GLY).[27,51,52,58]

674 We investigated the metabolic changes in PDTOs during treatment. Initially, PDTOs were
675 treated with a positive control drug for apoptotic cell death, staurosporine (STA), which is
676 a multi-kinase inhibitor, and stained with a vital dye, DRAQ7, to detect dead cells
677 (**Supplemental Figure S11**). Metabolic shifts towards OXPHOS were observed and co-
678 registered with positive staining of DRAQ7, indicating that in these PDTOs, a shift towards
679 OXPHOS correlated with cell death in response to drug treatment. In CRC media
680 conditions treated with various concentrations of 3-BP, there was no significant shift in
681 PDTO metabolic signatures detected by FLIM (**Figure 6A-B**) However, in CAF-CM
682 conditions treated with 3-BP, the metabolic signature shifted significantly towards
683 OXPHOS (increased fraction bound of NAD(P)H, or the ratio of NAD(P)H/NAD(P)+) at
684 the 80 and 100μM drug concentrations, with a concurrent increase in DRAQ7
685 fluorescence signal detected (indicating regions of cell death).

686 Since FLIM provides a measure of glycolysis and oxidative phosphorylation, we returned
687 to the computational model to calculate and compare the total GLY and OXPHOS fluxes.
688 When we compared the FLIM experimental results to predicted fluxes in the HK simulated
689 knockdown condition, the *in-silico* analysis was supported by our experimental findings.
690 Specifically, in CAF-CM conditions, the model shows that the ratio of glycolysis to
691 oxidative phosphorylation decreased, indicating a shift toward oxidative phosphorylation.
692 Furthermore, the model predicts increased glycolysis in the CRC media conditions
693 (**Figure 6C**). While this shift towards glycolysis does not quantitatively agree with the
694 FLIM results, the model predicts that 3-BP treatment alters these reaction fluxes in
695 opposite directions for CRC cells in CAF-CM versus CRC media.

696 In addition to the metabolic imaging readouts, we incorporated a cell viability assay (CTG)
697 based on intracellular ATP levels. The IC_{50} values of PDTOs treated with 3-BP in the CRC
698 or CAF-CM conditions were 40.93 μM and 86.96 μM, respectively (**Figure 6D and**
699 **Supplementary Table S1**), suggesting CAF-CM renders PTDOs more sensitive to HK
700 inhibition. We again returned to the model to generate calculations that can be directly
701 compared to the experimental measurements. Specifically, we considered the predicted
702 biomass rates from our model simulations with HK knockdown. As expected, the biomass
703 flux was significantly lower for CAF-CM compared to CRC media conditions (**Figure 6E**),
704 showing agreement between experiments and computational modeling predictions.

705 Additionally, we examined whether this effect was exclusive to HK inhibition or if it could
706 be attributed to a broader stress response by testing clinically relevant chemotherapy
707 drugs, including SN-38, an active metabolite of irinotecan, and 5-fluorouracil (5-FU). SN-
708 38 treatment in the CRC media condition showed a shift towards OXPHOS in a dose-
709 dependent manner after 72 hours of treatment and a positive DRAQ7 staining
710 (**Supplemental Figure S12A-B**); however, 5-FU did not show this metabolic effect. When
711 grown in CAF-CM, fraction bound values also shifted significantly towards OXPHOS at
712 higher concentrations of SN-38, and no change was seen when treated with 5-FU. IC_{50}

713 values from dose-response curves of PDTOs in CRC media conditions treated with SN-
714 38 or 5-FU were calculated to be 0.01 μM and 1.3 μM, respectively (**Supplementary**
715 **Table S1, Supplemental Figure S12**). In CAF-CM, the average IC_{50} values of PDTOs
716 treated with SN-38 and 5-FU were 0.005 μM and 2.31 μM, respectively. It is important to
717 note that DRCs with 5-FU treatment showed that the IC_{50}s for PDTOs in CAF-CM (2.03
718 μM) were significantly lower compared to when cultured in CRC media (23.93 μM);
719 however, among the six total (three in CAF-CM and three in CRC media) DRC
720 experiments for 5-FU, we never obtained an upper asymptote as defined by Sebaugh's[59]
721 bendpoint formula. Diluting 5-FU enough to obtain an upper asymptote was not feasible,
722 so we were only ever able to obtain at most two concentrations with a percent response
723 higher than 50%. Comparison between these IC_{50}s with Welch's *t*-test may be inaccurate
724 as seen in **Supplemental Figure S13C** where their confidence intervals overlap. Overall,
725 treatment with the chemotherapy agents did not result in a differential metabolic shift
726 between CRC and CAF-CM conditions, unlike what was observed with 3-BP treatment.

727 Discussion

728 Metabolic reprogramming of cancer cells has been linked to cancer progression and drug
729 resistance. For example, $KRAS^{MUT}$ colorectal cancer cells have been reported to have
730 increased activity of glycolysis, resulting in increased glucose uptake and lactate. This
731 metabolic reprogramming is correlated with altered cellular growth, and contributes to
732 invasion, metastasis, and drug resistance.[43,44,60] The TME has been shown to be a key
733 player in supporting these outcomes. Notably, CAFs have a metabolically dependent
734 relationship with tumor cells to promote the survival of each other.[5,6,60–62] Given the
735 influence of CAFs, it may be possible to exploit the CRC cell-CAF metabolic interactions
736 to inhibit tumor progression.

737 We have developed a novel, exploratory pipeline to systematically assess, in a high-
738 throughput manner, the comprehensive network effects of enzyme knockdowns in a
739 colorectal cancer-specific model of central carbon metabolism and CAF crosstalk. We
740 combine our *in-silico* predictions with experimental methods to validate our findings and
741 to better understand the effects of metabolic perturbations. Our integrated computational-
742 experimental pipeline identifies enzymes that would be potential therapeutic targets to
743 exploit CRC cell-CAF metabolic crosstalk. Our framework utilizes a representation
744 learning approach as a form of dimensionality reduction, as it captures the complexities
745 of our input data (fluxes through the entire metabolic network) and allows for meaningful
746 representation of the data in 2D space. We then utilize a distance-based metric to identify
747 influential perturbations that strongly alter the network flux, thus helping us to prioritize
748 experimental testing. Utilization of flux balance analysis on the constraint-based model
749 adapted by Wang *et al.* provides insight into the mechanisms by which CAFs trigger
750 extensive metabolic alterations in CRC.[21]

751

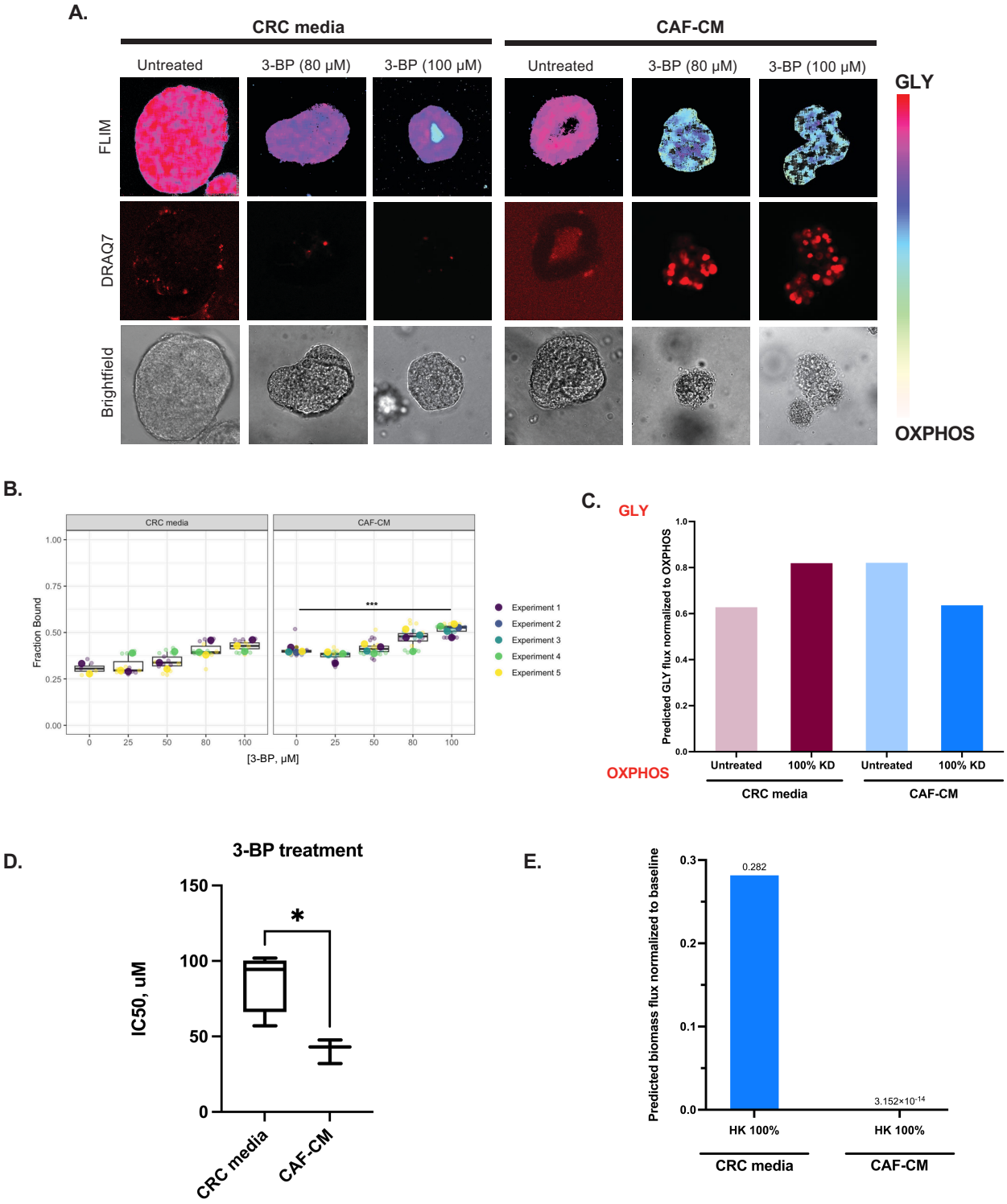

Figure 6: HK inhibition alters metabolic activity and cell viability in CAF-conditioned PDTOs. (A) Representative FLIM images and DRAQ7 staining of $KRAS^{MUT}$ PDTOs (000US) in control CRC media or patient-matched CAF-CM after 72 hours of 3-BP treatment. **(B)** Quantified metabolic signature values comparing PDTOs in CRC media and CAF-CM conditions with 3-BP treatment. For CAF-CM conditions n = 2-3 (2 for 0uM and 3 for 25-100uM). For CRC conditions: n= 4. ***p<0.001**(C)** Model-predicted metabolic signature values comparing cells in CRC media and CAF-CM with HK knockdown. **(D)** Calculated IC_{50} values from dose response curves of PDTOs treated with 3-BP in CRC media or CAF-CM. *p<0.05 **(E)**

Model-predicted biomass flux for full knockdown of HK in CRC media and CAF-CM normalized to baseline (no model perturbation).

Initial heatmap analysis of a single condition, $KRAS_{CAF}$, shows visible metabolic alterations following enzyme knockdowns. For example, glycolytic knockdowns have a more pronounced impact on metabolic fluxes than others. We can also observe the pronounced effects of inhibiting glycolysis on other pathways, as well as on metabolic transport and exchange. Our results also reveal certain enzymes, such as IDH, MDH and GDH, as highly sensitive to various knockdowns, underscoring their potential importance in regulating cellular metabolism.[63–65] This projection of data in 2D space revealed a clear separation among the four conditions. The $KRAS_{CAF}$ cluster distinctly isolates from the other three clusters, suggesting that CAFs uniquely alter the $KRAS^{MUT}$ cells significantly more than the $KRAS^{WT}$ cells and further supports the impact of CAFs on cancer cell metabolism as previously studied by Dias Carvalho *et al*.[66] Additionally, a clear separation between WT_{CAF} and $KRAS_{CAF}$ highlights genotype-dependent differences, but still a definite impact of CAFs.

We used Euclidean distance measurements within the clusters to identify metabolic perturbations. The resulting distributions of distances from the centroids for all four experimental conditions approximate a lightly tailed normal distribution, enhancing the statistical power of our method. By focusing on perturbations farthest from the mean, we can identify the influential knockdowns. Consistent with previous experimental and computational research, our model suggests that targeting enzymes such as HK, PYK, and LDH -- especially at higher levels, such as 80% or 100% knockdown -- can significantly inhibit metabolism and CRC cell growth. Moreover, overexpressing these enzymes results in cancer cells with enhanced resistance.[67,68] Furthermore, certain metabolic perturbations, such as GAPDH, LDH, and PYK, as well as G6PD, HK, HPI, and FUM2 cluster together. This indicates that inhibiting these reactions has a similar effect and suggests that they share regulatory characteristics on central carbon metabolism. For example, G6PD is a rate-limiting step in the PPP, while HK and HPI represent critical steps in glycolysis. Similarly, FUM2 acts as a bottleneck in the TCA cycle, as minor perturbations cause significant flux changes as detailed in previous experimental work.[69] Overall, our framework effectively pinpoints potential strategic interventions to achieve pre-defined, specific metabolic goals.

To experimentally validate our *in-silico* results, we used a label-free imaging-based approach to observe metabolic shifts in response to perturbations within $KRAS^{MUT}$ PDTOs. High-throughput quantitative experimental data is crucial for validating model predictions. However, a major challenge in the field of cancer metabolism is the ability to recreate complex metabolic interactions and patient-specific metabolism *in vitro*. Bioengineered cancer models, including PDTOs, offer unique opportunities for drug screening. These models leverage characteristics such as patient-level heterogeneity, high-throughput capabilities, and the ability to incorporate multiple cell types and other components of the TME.[55,61,70] Importantly, drug screening assays using PDTOs have

802 shown a strong positive correlation in their response with that observed in the
803 patient.[53,71,72]

804 Conventional assays often employed in these drug studies use end-point measurements
805 of viability based on a heterogeneous mixture of PDTOs. Imaging-based applications
806 provide a complementary method for screening, allowing dynamic measurements of drug
807 response. Coupling confocal imaging with vital dyes and brightfield imaging has
808 demonstrated the ability to capture additional information, including changes in growth
809 rates, heterocellular responses, individual organoid morphology, and discerning whether
810 a treatment is cytostatic or cytotoxic.[34,35,73] Moreover, FLIM enriches our understanding
811 of drug response by examining metabolic signatures within sub-cellular compartments
812 and quantifying the heterogeneity within the sample.[54–56,70,74] This label-free imaging
813 method can effectively capture metabolic changes over time. Each pixel of the
814 fluorescence emission signal of free NAD(P)H, an endogenous metabolite, is measured
815 and Fourier transformed. This yields a fit-free representation of the imaging data in the
816 form of a phasor plot.[26,57] The ratio of bound to free NAD(P)H is correlated to regions of
817 relative shifts in glycolysis and oxidative phosphorylation.[27,52,58,75] An advantage of using
818 FLIM to quantify drug response is the ability to detect drug effects earlier compared to the
819 use of vital dyes. We observed metabolic shifts towards OXPHOS in PDTOs treated with
820 SN-38 as early as 6 hours after treatment, although DRAQ7 staining was not evident until
821 later time points (**Supplemental Figure S14**).

822 When employing this experimental workflow, we demonstrated that pharmacological
823 inhibition of HK resulted in significant metabolic and viability changes in the CAF-CM
824 condition, which corroborated our *in-silico* HK knockdown simulations. This aligns with
825 research demonstrating that HK is essential for the survival of cancer cells and
826 significantly impacts tumor progression.[76] To further exhibit that HK2 was a vulnerable
827 enzyme within the CAF-CM setting, we repeated our experiments with two clinically
828 relevant chemotherapy agents. In contrast to our findings with 3-BP treatment, where only
829 the CAF-CM condition exhibited the highest sensitivity to HK inhibition, PDTOs responded
830 similarly to SN-38 in both the CRC media and CAF-CM conditions, showing a shift
831 towards OXPHOS at the highest drug concentrations. Previous studies have shown
832 treatment with irinotecan in $KRAS^{MUT}$ cells resulted in an increase in mitochondria activity,
833 which supports our measured OXPHOS signature. [77] Additionally, it has been shown that
834 treatment of CRC cells with irinotecan can result in a decrease in hexokinase activity[78],
835 which could explain the viability similarities between the 3-BP and SN-38 treatments.
836 Interestingly, 5-FU, a pyrimidine antimetabolite effective in clinical settings, resulted in a
837 decrease in organoid viability in our measurements, yet there was no apparent impact on
838 the main pathways within central carbon metabolism, as indicated by the lack of GLY-
839 OXPHOS metabolic shifts in either the CRC media or CAF-CM conditions from FLIM
840 analysis. Future work exploring dual targeting of glucose and pyrimidine metabolism may
841 enhance the sensitivity of colorectal cancer cells. Overall, our findings suggest that CRC
842 cell-CAF metabolic interactions are more sensitive to targeting HK2, resulting in an
843 enhanced therapeutic response.

844 ***Limitations.*** We acknowledge some limitations in our study that are important to consider
845 in future research. Primarily, our model is limited to central carbon metabolism. While
846 insightful, this captures a small percentage of cellular metabolism and leaves out
847 pathways and reactions that could play pivotal roles in, or be affected by, the enzyme
848 knockdowns we analyzed. Excluded reactions also lead to compensatory mechanisms in
849 the metabolic network that we cannot consider. Future studies may utilize a genome-
850 scale model (GEM) that encapsulates the entirety of human metabolic reactions for a
851 particular cell type. This would facilitate a more thorough understanding of metabolic
852 reprogramming. Moreover, our model is influenced by environmental factors present in
853 the experimental studies, limiting its universal applicability: the conditions under which
854 our experiments were conducted, specifically the glucose, lactate, and glutamine uptake
855 and secretion rates, greatly shape the predicted fluxes. As such, these findings may not
856 be directly transposable across different cell lines or experimental setups. Future work
857 can consider alternate nutrient sources and growth conditions. Moreover, our current
858 study concentrates on the influence of CAF-secreted factors using conditioned media,
859 with follow-up investigations exploring the potential of physical interactions using co-
860 culture models. Moreover, we recognize the limitations of our selected inhibitor, 3-BP,
861 when experimentally validating our computational findings. Although 3-BP is effective at
862 limiting HK2 activity, it, like many pharmacological agents, may interfere with and
863 suppress other biochemical pathways, potentially leading to unintended off-target effects.
864 Future work can utilize more precise targeting of HK2 activity.

865

866 ***Conclusions.*** Overall, we demonstrate the utility of our integrated computational-
867 experimental approach for identifying perturbations that exploit metabolic crosstalk
868 between CRC cells and CAFs. Importantly, we show that the model predictions can be
869 validated experimentally using FLIM and conventional cell viability assays. Our
870 established pipeline is versatile and can be integrated with other constraint-based
871 colorectal cancer models, such as GEMs. The approach is also flexible, allowing the
872 inclusion of additional pathways and facilitating double-enzyme knockdown simulations
873 and combinatorial drug treatments. Thus, our work is a foundation for identifying effective
874 strategies for targeting cancer metabolism.

875 Acknowledgements

876 We would like to thank the members of the Ellison Institute of Technology and Finley Lab
877 at USC for the deep scientific discussions. Special thanks to Scott Valena and Pratiksha
878 Kshetri for cell culture assistance, Nolan Ung for statistical guidance, the Translational
879 Imaging Center at USC for providing us usage of their microscope systems, and the USC
880 Norris Comprehensive Cancer Center Translational Pathology Core for the collection of
881 patient tissue samples (Norris Comprehensive Cancer Center CCSG grant,
882 P30CA014089). We would also like to thank the National Cancer Institute Cancer
883 Systems Biology Consortium for funding this project (U01-CA-232137).

Author contributions

N.T. conducted all metabolic modeling and computational analyses. E.J.F. conducted or directed all experimental sample preparation, data collection, and analysis for FLIM experiments, cell viability measurements, and hexokinase activity assays. FLIM imaging and data analysis was also done by Y.K.H. M.B. collected CTG and FLIM organoid data. Image-based quality control and experimental planning was done by M.D. and S.K. A.C. performed quality control analysis of all CellTiter-Glo and FLIM experiments and calculations of IC_{50} values. HJL provided CRC patient samples and clinical expertise. E.J.F., N.T., S.M.M., P.M., N.A.G., and S.D.F. contributed to manuscript writing and scientific discussions of results. S.M.M. and S.D.F. were responsible for the scientific direction of this work. All authors reviewed and provided feedback on the manuscript.

Declaration of interests

The authors declare no conflict of interest.

References

1. Luengo, A., Gui, D.Y., and Vander Heiden, M.G. (2017). Targeting Metabolism for Cancer Therapy. Cell Chem. Biol. *24*, 1161–1180. https://doi.org/10.1016/j.chembiol.2017.08.028.

2. Hanahan, D. (2022). Hallmarks of Cancer: New Dimensions. Cancer Discov. *12*, 31–46. https://doi.org/10.1158/2159-8290.CD-21-1059.

3. Pavlova, N.N., Zhu, J., and Thompson, C.B. (2022). The hallmarks of cancer metabolism: Still emerging. Cell Metab. *34*, 355–377. https://doi.org/10.1016/j.cmet.2022.01.007.

4. Karta, J., Bossicard, Y., Kotzamanis, K., Dolznig, H., and Letellier, E. (2021). Mapping the Metabolic Networks of Tumor Cells and Cancer-Associated Fibroblasts. Cells *10*, 1–25. https://doi.org/10.3390/CELLS10020304.

5. Patel, B.B., Ackerstaff, E., Serganova, I.S., Kerrigan, J.E., Blasberg, R.G., Koutcher, J.A., and Banerjee, D. (2017). Tumor stroma interaction is mediated by monocarboxylate metabolism. Exp. Cell Res. *352*, 20–33. https://doi.org/10.1016/J.YEXCR.2017.01.013.

6. Pavlides, S., Whitaker-Menezes, D., Castello-Cros, R., Flomenberg, N., Witkiewicz, A.K., Frank, P.G., Casimiro, M.C., Wang, C., Fortina, P., Addya, S., et al. (2009). The reverse Warburg effect: aerobic glycolysis in cancer associated fibroblasts and the tumor stroma. Cell Cycle Georget. Tex *8*, 3984–4001. https://doi.org/10.4161/CC.8.23.10238.

7. Rahman, M., and Hasan, M.R. (2015). Cancer Metabolism and Drug Resistance. Metab. 2015 Vol 5 Pages 571-600 *5*, 571–600. https://doi.org/10.3390/METABO5040571.

8. Shin, Y.K., Yoo, B.C., Hong, Y.S., Chang, H.J., Jung, K.H., Jeong, S.Y., and Park, J.G. (2009). Upregulation of glycolytic enzymes in proteins secreted from human colon cancer cells with 5-fluorouracil resistance. Electrophoresis *30*, 2182–2192. https://doi.org/10.1002/ELPS.200800806.

9. Curvello, R., Berndt, N., Hauser, S., and Loessner, D. (2024). Recreating metabolic interactions of the tumour microenvironment. Trends Endocrinol. Metab., S1043276023002503. https://doi.org/10.1016/j.tem.2023.12.005.

10. Medina, M.Á. (2018). Mathematical modeling of cancer metabolism. Crit. Rev. Oncol. Hematol. *124*, 37–40. https://doi.org/10.1016/j.critrevonc.2018.02.004.

11. Rockne, R.C., Hawkins-Daarud, A., Swanson, K.R., Sluka, J.P., Glazier, J.A., Macklin, P., Hormuth, D.A., Jarrett, A.M., Lima, E.A.B.F., Tinsley Oden, J., et al. (2019). The 2019 mathematical oncology roadmap. Phys. Biol. *16*, 041005. https://doi.org/10.1088/1478-3975/ab1a09.

12. Roy, M., and Finley, S.D. (2017). Computational Model Predicts the Effects of Targeting Cellular Metabolism in Pancreatic Cancer. Front. Physiol. *8*.

13. Metzcar, J., Wang, Y., Heiland, R., and Macklin, P. (2019). A Review of Cell-Based Computational Modeling in Cancer Biology. JCO Clin. Cancer Inform., 1–13. https://doi.org/10.1200/CCI.18.00069.

14. Lapin, A., Perfahl, H., Jain, H.V., and Reuss, M. (2022). Integrating a dynamic central metabolism model of cancer cells with a hybrid 3D multiscale model for vascular hepatocellular carcinoma growth. Sci. Rep. *12*, 12373. https://doi.org/10.1038/s41598-022-15767-6.

15. Roy, M., and Finley, S.D. (2019). Metabolic reprogramming dynamics in tumor spheroids: Insights from a multicellular, multiscale model. PLOS Comput. Biol. *15*, e1007053. https://doi.org/10.1371/journal.pcbi.1007053.

16. Aurich, M.K., Fleming, R.M.T., and Thiele, I. (2016). MetaboTools: A Comprehensive Toolbox for Analysis of Genome-Scale Metabolic Models. Front. Physiol. *7*, 327. https://doi.org/10.3389/fphys.2016.00327.

17. Dai, Z., and Locasale, J.W. (2017). Understanding metabolism with flux analysis: From theory to application. Metab. Eng. *43*, 94–102. https://doi.org/10.1016/j.ymben.2016.09.005.

18. Khaleghi, M.K., Savizi, I.S.P., Lewis, N.E., and Shojaosadati, S.A. (2021). Synergisms of machine learning and constraint-based modeling of metabolism for analysis and optimization of fermentation parameters. Biotechnol. J. *16*, 2100212. https://doi.org/10.1002/biot.202100212.

19. Orth, J.D., Thiele, I., and Palsson, B.Ø. (2010). What is flux balance analysis? Nat. Biotechnol. *28*, 245–248. https://doi.org/10.1038/nbt.1614.

20. Gatto, F., Miess, H., Schulze, A., and Nielsen, J. (2015). Flux balance analysis predicts essential genes in clear cell renal cell carcinoma metabolism. Sci. Rep. *5*, 10738. https://doi.org/10.1038/srep10738.

21. Wang, J., Delfarah, A., Gelbach, P., Fong, E., Macklin, P., Mumenthaler, S.M., Graham, N.A., and Finley, S. (2022). Elucidating tumor-stromal metabolic crosstalk in colorectal cancer through integration of constraint-based models and LC-MS metabolomics. Metab. Eng. https://doi.org/10.1016/J.YMBEN.2021.11.006.

22. Cess, C.G., and Finley, S.D. (2023). Calibrating agent-based models to tumor images using representation learning. PLOS Comput. Biol. *19*, e1011070. https://doi.org/10.1371/journal.pcbi.1011070.

23. Schutgens, F., and Clevers, H. (2020). Human Organoids: Tools for Understanding Biology and Treating Diseases. Annu. Rev. Pathol. Mech. Dis. *15*, 2129253558. https://doi.org/10.1146/annurev-pathmechdis-012419-032611.

24. Clevers, H., and Tuveson, D.A. (2019). Organoid Models for Cancer Research. Annu. Rev. Cancer Biol. *3*, 223–234. https://doi.org/10.1146/annurev-cancerbio-030518-055702.

975 25. Van De Wetering, M., Francies, H.E., Francis, J.M., Bounova, G., Iorio, F., Pronk,
976 A., Van Houdt, W., Van Gorp, J., Taylor-Weiner, A., Kester, L., et al. (2015).
977 Prospective derivation of a living organoid biobank of colorectal cancer patients. Cell
978 *161*, 933–945. https://doi.org/10.1016/j.cell.2015.03.053.

979 26. Ranjit, S., Malacrida, L., Jameson, D.M., and Gratton, E. (2018). Fit-free analysis of
980 fluorescence lifetime imaging data using the phasor approach. Nat. Protoc. *13*,
981 1979–2004. https://doi.org/10.1038/s41596-018-0026-5.

982 27. Stringari, C., Edwards, R.A., Pate, K.T., Waterman, M.L., Donovan, P.J., and
983 Gratton, E. (2012). Metabolic trajectory of cellular differentiation in small intestine by
984 Phasor Fluorescence Lifetime Microscopy of NADH. Sci. Rep. *2*.
985 https://doi.org/10.1038/srep00568.

986 28. Raue, A., Schilling, M., Bachmann, J., Matteson, A., Schelke, M., Kaschek, D., Hug,
987 S., Kreutz, C., Harms, B.D., Theis, F.J., et al. (2013). Lessons Learned from
988 Quantitative Dynamical Modeling in Systems Biology. PLoS ONE *8*, e74335.
989 https://doi.org/10.1371/journal.pone.0074335.

990 29. Lewis, N.E., Hixson, K.K., Conrad, T.M., Lerman, J.A., Charusanti, P., Polpitiya,
991 A.D., Adkins, J.N., Schramm, G., Purvine, S.O., Lopez-Ferrer, D., et al. (2010).
992 Omic data from evolved E. coli are consistent with computed optimal growth from
993 genome-scale models. Mol. Syst. Biol. *6*, 390. https://doi.org/10.1038/msb.2010.47.

994 30. Chicco, D. (2021). Siamese Neural Networks: An Overview. In Artificial Neural
995 Networks Methods in Molecular Biology., H. Cartwright, ed. (Springer US), pp. 73–
996 94. https://doi.org/10.1007/978-1-0716-0826-5_3.

997 31. Maaten, L. van der, and Hinton, G. (2008). Visualizing Data using t-SNE. J. Mach.
998 Learn. Res. *9*, 2579–2605.

999 32. Bengio, Y., Courville, A., and Vincent, P. (2014). Representation Learning: A Review
1000 and New Perspectives. Preprint at arXiv.

1001 33. Szubert, B., Cole, J.E., Monaco, C., and Drozdov, I. (2019). Structure-preserving
1002 visualisation of high dimensional single-cell datasets. Sci. Rep. *9*, 8914.
1003 https://doi.org/10.1038/s41598-019-45301-0.

1004 34. Garvey, C.M., Lau, R., Sanchez, A., Sun, R.X., Fong, E.J., Doche, M.E., Chen, O.,
1005 Jusuf, A., Lenz, H.J., Larson, B., et al. (2020). Anti-EGFR therapy induces EGF
1006 secretion by cancer-associated fibroblasts to confer colorectal cancer
1007 chemoresistance. Cancers *12*. https://doi.org/10.3390/cancers12061393.

1008 35. Kim, S., Choung, S., Sun, R.X., Ung, N., Hashemi, N., Fong, E.J., Lau, R., Spiller,
1009 E., Gasho, J., Foo, J., et al. (2020). Comparison of Cell and Organoid-Level
1010 Analysis of Patient-Derived 3D Organoids to Evaluate Tumor Cell Growth Dynamics
1011 and Drug Response. Slas Discov. *25*, 744.
1012 https://doi.org/10.1177/2472555220915827.

1013 36. R Core Team R: A Language and Environment for Statistical Computing. (R
1014 Foundation for Statistical Computing).

1015 37. Stopsack, K., and Gerke, T. (2021). _batchtma: Batch Effect Adjustments_. Version
1016 R package version 0.1.6.

1017 38. Postit Team (2023). RStudio: Integrated Development Environment for R. (Postit).

1018 39. Ritz, C., Baty, F., Streibig, J.C., and Gerhard, D. (2015). Dose-Response Analysis
1019 Using R. PLOS ONE *10*, e0146021. https://doi.org/10.1371/journal.pone.0146021.

1020 40. Zhang, J.H., Chung, T.D., and Oldenburg, K.R. (1999). A Simple Statistical
1021 Parameter for Use in Evaluation and Validation of High Throughput Screening
1022 Assays. J. Biomol. Screen. *4*, 67–73. https://doi.org/10.1177/108705719900400206.

1023 41. Iversen, P.W., Beck, B., Chen, Y.-F., Dere, W., Devanarayan, V., Eastwood, B.J.,
1024 Farmen, M.W., Iturria, S.J., Montrose, C., Moore, R.A., et al. (2004). HTS Assay
1025 Validation. In Assay Guidance Manual, S. Markossian, A. Grossman, K.
1026 Brimacombe, M. Arkin, D. Auld, C. Austin, J. Baell, T. D. Y. Chung, N. P. Coussens,
1027 J. L. Dahlin, et al., eds. (Eli Lilly & Company and the National Center for Advancing
1028 Translational Sciences).

1029 42. Wang, J., Delfarah, A., Gelbach, P.E., Fong, E., Macklin, P., Mumenthaler, S.M.,
1030 Graham, N.A., and Finley, S.D. (2022). Elucidating tumor-stromal metabolic
1031 crosstalk in colorectal cancer through integration of constraint-based models and
1032 LC-MS metabolomics. Metab. Eng. *69*, 175–187.
1033 https://doi.org/10.1016/j.ymben.2021.11.006.

1034 43. Ham, I.H., Lee, D., and Hur, H. (2021). Cancer-associated fibroblast-induced
1035 resistance to chemotherapy and radiotherapy in gastrointestinal cancers. Cancers
1036 *13*, 1–17. https://doi.org/10.3390/cancers13051172.

1037 44. Tommelein, J., Verset, L., Boterberg, T., Demetter, P., Bracke, M., and De Wever,
1038 O. (2015). Cancer-Associated Fibroblasts Connect Metastasis-Promoting
1039 Communication in Colorectal Cancer. Front. Oncol. *5*, 63.
1040 https://doi.org/10.3389/fonc.2015.00063.

1041 45. Ho, N., Morrison, J., Silva, A., and Coomber, B.L. (2016). The effect of 3-
1042 bromopyruvate on human colorectal cancer cells is dependent on glucose
1043 concentration but not hexokinase II expression. Biosci. Rep. *36*, 299.
1044 https://doi.org/10.1042/BSR20150267/56385.

1045 46. Ho, N., and Coomber, B.L. (2016). Hexokinase II expression is correlated with
1046 colorectal cancer prognosis. Cancer Treat. Commun. *6*, 11–16.
1047 https://doi.org/10.1016/J.CTRC.2016.02.008.

1048 47. Li, J., Pan, J., Liu, Y., Luo, X., Yang, C., Xiao, W., Li, Q., Yang, L., and Zhang, X.
1049 (2022). 3-Bromopyruvic acid regulates glucose metabolism by targeting the
1050 c-Myc/TXNIP axis and induces mitochondria-mediated apoptosis in TNBC cells.
1051 Exp. Ther. Med. *24*, 1–11. https://doi.org/10.3892/etm.2022.11447.

1052 48. Wu, J., Hu, L., Wu, F., Zou, L., and He, T. (2017). Poor prognosis of hexokinase 2
1053 overexpression in solid tumors of digestive system: a meta-analysis. Oncotarget *8*,
1054 32332. https://doi.org/10.18632/ONCOTARGET.15974.

1055 49. Rempel, A., Mathupala, S.P., Griffin, C.A., Hawkins, A.L., and Pedersen, P.L.
1056 (1996). Glucose catabolism in cancer cells: amplification of the gene encoding type
1057 II hexokinase. Cancer Res. *56*, 2468–2471.

1058 50. Datta, R., Sivanand, S., Lau, A.N., Florek, L.V., Barbeau, A.M., Wyckoff, J., Skala,
1059 M.C., and Heiden, M.G.V. (2022). Interactions with stromal cells promote a more
1060 oxidized cancer cell redox state in pancreatic tumors. Sci. Adv. *8*, 6383.
1061 https://doi.org/10.1126/SCIADV.ABG6383.

1062 51. Ma, N., Mochel, N.R., Pham, P.D., Yoo, T.Y., Cho, K.W.Y., and Digman, M.A.
1063 (2019). Label-free assessment of pre-implantation embryo quality by the
1064 Fluorescence Lifetime Imaging Microscopy (FLIM)-phasor approach. Sci. Rep. *9*.
1065 https://doi.org/10.1038/s41598-019-48107-2.

1066 52. Mah, E.J., Lefebvre, A.E.Y.T., McGahey, G.E., Yee, A.F., and Digman, M.A. (2018).
1067 Collagen density modulates triple-negative breast cancer cell metabolism through
1068 adhesion-mediated contractility. Sci. Rep. *8*, 17094. https://doi.org/10.1038/s41598-
1069 018-35381-9.

1070 53. Pasch, C.A., Favreau, P.F., Yueh, A.E., Babiarz, C.P., Gillette, A.A., Sharick, J.T.,
1071 Karim, M.R., Nickel, K.P., DeZeeuw, A.K., Sprackling, C.M., et al. (2019). Patient-
1072 derived cancer organoid cultures to predict sensitivity to chemotherapy and
1073 radiation. Clin. Cancer Res. Off. J. Am. Assoc. Cancer Res. *25*, 5376.
1074 https://doi.org/10.1158/1078-0432.CCR-18-3590.

1075 54. Shah, A.T., Heaster, T.M., and Skala, M.C. (2017). Metabolic Imaging of Head and
1076 Neck Cancer Organoids. PloS One *12*.
1077 https://doi.org/10.1371/JOURNAL.PONE.0170415.

1078 55. Skala, M.C., Deming, D.A., and Kratz, J.D. (2022). Technologies to Assess Drug
1079 Response and Heterogeneity in Patient-Derived Cancer Organoids. Annu. Rev.
1080 Biomed. Eng. *24*. https://doi.org/10.1146/ANNUREV-BIOENG-110220-123503.

1081 56. Zagaynova, E.V., Shirmanova, M.V., Lukina, M., Dudenkova, V., Elagin, V., Shlivko,
1082 I., Shcheslavskiy, V.I., Ignatova, N., and Orlinskay, N. (2018). Metabolic imaging of
1083 tumor for diagnosis and response for therapy. In Multiphoton Microscopy in the
1084 Biomedical Sciences XVIII, A. Periasamy, P. T. So, X. S. Xie, and K. König, eds.
1085 (SPIE), p. 3. https://doi.org/10.1117/12.2295127.

1086 57. Digman, M.A., Caiolfa, V.R., Zamai, M., and Gratton, E. (2008). The phasor
1087 approach to fluorescence lifetime imaging analysis. Biophys. J. *94*.
1088 https://doi.org/10.1529/biophysj.107.120154.

1089 58. Sameni, S., Syed, A., Marsh, J.L., and Digman, M.A. (2016). The phasor-FLIM
1090 fingerprints reveal shifts from OXPHOS to enhanced glycolysis in Huntington
1091 Disease. Sci. Rep. *6*, 34755. https://doi.org/10.1038/srep34755.

1092 59. Sebaugh, J.L. (2011). Guidelines for accurate EC50/IC50 estimation. Pharm. Stat.
1093 *10*, 128–134. https://doi.org/10.1002/pst.426.

1094 60. Martinez-Outschoorn, U.E., Lisanti, M.P., and Sotgia, F. (2014). Catabolic cancer-
1095 associated fibroblasts transfer energy and biomass to anabolic cancer cells, fueling
1096 tumor growth. Semin. Cancer Biol. *25*, 47–60.
1097 https://doi.org/10.1016/J.SEMCANCER.2014.01.005.

1098 61. Ramos Zapatero, M., Tong, A., Sufi, J., Vlckova, P., Cardoso, F., Nattress, C., Qin,
1099 X., Hochhauser, D., Krishnaswamy, S., and Tape, J. Trellis Single-Cell Screening
1100 Reveals Stromal Regulation of Patient-Derived Organoid Drug Responses.
1101 https://doi.org/10.1101/2022.10.19.512668.

1102 62. Schuth, S., Le Blanc, S., Krieger, T.G., Jabs, J., Schenk, M., Giese, N.A., Büchler,
1103 M.W., Eils, R., Conrad, C., and Strobel, O. (2022). Patient-specific modeling of
1104 stroma-mediated chemoresistance of pancreatic cancer using a three-dimensional
1105 organoid-fibroblast co-culture system. J. Exp. Clin. Cancer Res. CR *41*, 312.
1106 https://doi.org/10.1186/s13046-022-02519-7.

1107 63. Karaca, M., Frigerio, F., and Maechler, P. (2011). From pancreatic islets to central
1108 nervous system, the importance of glutamate dehydrogenase for the control of
1109 energy homeostasis. Neurochem. Int. *59*, 510–517.
1110 https://doi.org/10.1016/j.neuint.2011.03.024.

1111 64. Smith, H.Q., Li, C., Stanley, C.A., and Smith, T.J. (2019). Glutamate
1112 Dehydrogenase, a Complex Enzyme at a Crucial Metabolic Branch Point.
1113 Neurochem. Res. *44*, 117–132. https://doi.org/10.1007/s11064-017-2428-0.

1114 65. Walsh, K., and Koshland, D.E. (1985). Branch point control by the phosphorylation
1115 state of isocitrate dehydrogenase. A quantitative examination of fluxes during a
1116 regulatory transition. J. Biol. Chem. *260*, 8430–8437. https://doi.org/10.1016/S0021-
1117 9258(17)39492-9.

1118 66. Dias Carvalho, P., Mendonça, S., Martins, F., Oliveira, M.J., and Velho, S. (2022).
1119 Modulation of Fibroblast Phenotype by Colorectal Cancer Cell-Secreted Factors Is
1120 Mostly Independent of Oncogenic KRAS. Cells *11*, 2490.
1121 https://doi.org/10.3390/cells11162490.

1122 67. Manerba, M., Di Ianni, L., Govoni, M., Roberti, M., Recanatini, M., and Di Stefano,
1123 G. (2017). Lactate dehydrogenase inhibitors can reverse inflammation induced
1124 changes in colon cancer cells. Eur. J. Pharm. Sci. *96*, 37–44.
1125 https://doi.org/10.1016/j.ejps.2016.09.014.

1126 68. Zhou, C.-F., Li, X.-B., Sun, H., Zhang, B., Han, Y.-S., Jiang, Y., Zhuang, Q.-L.,
1127 Fang, J., and Wu, G.-H. (2012). Pyruvate kinase type M2 is upregulated in
1128 colorectal cancer and promotes proliferation and migration of colon cancer cells.
1129 IUBMB Life *64*, 775–782. https://doi.org/10.1002/iub.1066.

1130 69. Raimundo, N., Ahtinen, J., Fumić, K., Barić, I., Remes, A.M., Renkonen, R., Lapatto,
1131 R., and Suomalainen, A. (2008). Differential metabolic consequences of fumarate

1132 hydratase and respiratory chain defects. Biochim. Biophys. Acta - Mol. Basis Dis.
1133 *1782*, 287. https://doi.org/10.1016/j.bbadis.2008.01.008.

1134 70. Cannon, T.M., Shah, A.T., and Skala, M.C. (2017). Autofluorescence imaging
1135 captures heterogeneous drug response differences between 2D and 3D breast
1136 cancer cultures. Biomed. Opt. Express *8*, 1911–1925.
1137 https://doi.org/10.1364/BOE.8.001911.

1138 71. Bleijs, M., Wetering, M., Clevers, H., and Drost, J. (2019). Xenograft and organoid
1139 model systems in cancer research. EMBO J.
1140 https://doi.org/10.15252/embj.2019101654.

1141 72. Wensink, G.E., Elias, S.G., Mullenders, J., Koopman, M., Boj, S.F., Kranenburg,
1142 O.W., and Roodhart, J.M.L. (2021). Patient-derived organoids as a predictive
1143 biomarker for treatment response in cancer patients. Npj Precis. Oncol. *5*.
1144 https://doi.org/10.1038/s41698-021-00168-1.

1145 73. Garvey, C.M., Spiller, E., Lindsay, D., Chiang, C.T., Choi, N.C., Agus, D.B., Mallick,
1146 P., Foo, J., and Mumenthaler, S.M. (2016). A high-content image-based method for
1147 quantitatively studying context-dependent cell population dynamics. Sci. Rep. *6*.
1148 https://doi.org/10.1038/srep29752.

1149 74. Gil, D.A., Deming, D., and Skala, M.C. (2021). Patient-derived cancer organoid
1150 tracking with wide-field one-photon redox imaging to assess treatment response. J.
1151 Biomed. Opt. *26*. https://doi.org/10.1117/1.jbo.26.3.036005.

1152 75. Stringari, C., Cinquin, A., Cinquin, O., Digman, M.A., Donovan, P.J., and Gratton, E.
1153 (2011). Phasor approach to fluorescence lifetime microscopy distinguishes different
1154 metabolic states of germ cells in a live tissue. Proc. Natl. Acad. Sci. U. S. A. *108*,
1155 13582–13587. https://doi.org/10.1073/pnas.1108161108.

1156 76. Patra, K.C., Wang, Q., Bhaskar, P.T., Miller, L., Wang, Z., Wheaton, W., Chandel,
1157 N., Laakso, M., Muller, W.J., Allen, E.L., et al. (2013). Hexokinase 2 is required for
1158 tumor initiation and maintenance and its systemic deletion is therapeutic in mouse
1159 models of cancer. Cancer Cell *24*, 213–228.
1160 https://doi.org/10.1016/j.ccr.2013.06.014.

1161 77. Marx, C., Sonnemann, J., Maddocks, O.D.K., Marx-Blümel, L., Beyer, M., Hoelzer,
1162 D., Thierbach, R., Maletzki, C., Linnebacher, M., Heinzel, T., et al. (2022). Global
1163 metabolic alterations in colorectal cancer cells during irinotecan-induced DNA
1164 replication stress. Cancer Metab. *10*, 10. https://doi.org/10.1186/s40170-022-00286-
1165 9.

1166 78. Sharma, R.I., and Smith, T.A.D. (2008). Colorectal Tumor Cells Treated with 5-FU,
1167 Oxaliplatin, Irinotecan, and Cetuximab Exhibit Changes in 18F-FDG Incorporation
1168 Corresponding to Hexokinase Activity and Glucose Transport. J. Nucl. Med.
1169 https://doi.org/10.2967/jnumed.107.047886.

1170